Engineering Geology 327 (2023) 107364

Contents lists available at ScienceDirect

Engineering Geology

journal homepage: www.elsevier.com/locate/enggeo

Deterministic seismic hazard analysis from physics-based earthquake simulations in the Eastern Betics (SE Iberia)

Paula Herrero-Barbero [a,*,1], José A. Álvarez-Gómez [a], Meaza Tsige [a], José J. Martínez-Díaz [a,b]

[a] Department of Geodynamics, Stratigraphy and Paleontology, Faculty of Geological Sciences, Complutense University of Madrid, Madrid, Spain
[b] IGEO, Geosciences Institute, CSIC-UCM, Madrid, Spain

ARTICLE INFO

Keywords:
Deterministic seismic hazard analysis
Physics-based earthquake simulator
Soil amplification
Geotechnical site classification
Eastern Betics

ABSTRACT

The low frequency of large destructive earthquakes in the Eastern Betics (SE Iberian Peninsula), not recorded in the instrumental seismic catalog, complicate the estimation of the maximum ground motion that could be reached. Knowing the characteristics and behavior of these large seismic ruptures is crucial for the study of seismic hazard. In this work, we have used a physics-based earthquake simulator to generate a 100 kyr catalog of seismic ruptures associated with seismogenic faults bordering the quaternary Guadalentin and Bajo Segura basins. From these ruptures, we have selected maximum earthquake scenarios, and those associated with certain probabilities of exceeding a severe magnitude from the synthetic catalog. The estimation of maximum peak accelerations (PGA) by means of ground motion prediction equations include a possible site amplification that we have calculated from a detailed geotechnical classification of soils. According to the simulations, the modeled faults have the capacity to generate maximum earthquakes with magnitudes ranging M_W 6.7–7.4. Densely populated urban areas located along the Guadalentin valley, such as Lorca, could be subject to site-dependent PGA values close to 0.6 g on the Alhama de Murcia fault trace. Similar ground motion would affect the coastline of SE Alicante province when evaluating the maximum simulated event in the Bajo Segura offshore fault. But already from magnitudes around $M_W \sim 6$, PGA estimations exceed critical values of 0.5 g at the south side of the Bajo Segura basin and the city of Murcia, highly dependent of ground-motion amplification induced by thick deposits of very soft and saturated soils. Our scenarios reflect that other factors such as fault geometry, kinematics and the capability observed in the simulations to generate multi-fault ruptures also affect the spatial distribution of maximum ground motion in this region. We expect that this evaluation could contribute as an improvement guideline for future strong motion prediction studies prior to the settlement of new urban infrastructures in the Eastern Betics.

1. Introduction

The seismicity in the Eastern Betic Cordillera (SE Iberian Peninsula), although moderate, form part of the circum-mediterranean seismic rim (Fig. 1a), with up to 10 destructive earthquakes with estimated macroseismic intensities greater than VIII since the 15th century (IGN-UPM, 2013; Martínez-Solares and Mezcua, 2002), which should be associated with peak ground accelerations (PGA) larger than 0.4 g (Worden et al., 2012). The 2011 Lorca earthquake (SE Spain), which caused nine fatalities, >300 injured and significant material damage despite its moderate magnitude M_W 5.1 and intensity VI (López-Comino et al., 2012; Martínez-Díaz et al., 2011; Martínez-Díaz et al., 2012a), highlighted the urgency of reinforcing the seismic hazard assessment in the area. Besides the 2011 Lorca instrumental event, most of these great earthquakes occurred in the Eastern Betics were located along the Guadalentin depression and the southern side of the Bajo Segura basin (Fig. 1a). A large number of urban centers are located on these Quaternary basins, being a densely populated area with over 750 k inhabitants.

Earthquake activity in this region is mostly related to the Eastern Betic Fault Zone (EBFZ; De Larouzière et al., 1988; Bousquet, 1979), a left-lateral tectonic corridor that crosses the southeast of the Iberian Peninsula (Fig. 1a) and bounds Mesozoic mountain ranges from Alpujárride and Maláguide tectonic complexes, and large Neogene and Quaternary sedimentary basins (Fig. 1b). This characteristic

* Corresponding author.
E-mail address: pherrero@geo3bcn.csic.es (P. Herrero-Barbero).
[1] Present address: Geosciences Barcelona (GEO3BCN-CSIC), Barcelona, Spain.

https://doi.org/10.1016/j.enggeo.2023.107364
Received 12 August 2022; Received in revised form 4 September 2023; Accepted 13 November 2023
Available online 15 November 2023

morphology is the result of a complex tectonic evolution in the western Mediterranean driven by the convergence between the Eurasian and African plates, in which the formation of the Miocene basins in an extensional stage (Meijninger and Vissers, 2006; Montenat and d'Estevou, 1999; Sanz de Galdeano, 1990) is followed by a compressional stress field with a dominant NNW-SSE shortening direction at a rate of 4 to 6 mm/yr (e.g., Fernandes et al., 2007; Koulali et al., 2011; Nocquet, 2012).

The Guadalentin and Bajo Segura basins are located at the northern end of this fault zone (Fig. 1c). These basins were formed as a consequence of the tectonic inversion of the structures flanking the valleys induced by the compressional regime, as a pop-down structure in the case of the Guadalentín basin (Martínez-Díaz et al., 2001) and related to growth folding in the Bajo Segura basin (Alfaro et al., 2002). Both basins are fault-controlled, with estimated fault slip rates <1.5 mm/yr (Alfaro et al., 2012; Booth-Rea et al., 2004; Ferrater et al., 2017; Gómez-Novell et al., 2022; Herrero-Barbero et al., 2020; Insua-Arévalo et al., 2015; Martín-Banda et al., 2021; Moreno et al., 2015; Ortuño et al., 2012). The Guadalentin basin is bounded by NNE–SSW to NE strike-slip structures with some reverse component (Fig. 1a): the Palomares fault (PF; Booth-Rea et al., 2004; Bousquet, 1979), the Alhama de Murcia fault (AMF; Martínez-Díaz et al., 2012b; Montenat, 1973), the Los Tollos fault (LTF; Insua-Arévalo et al., 2015) and the Carrascoy fault (CAF; Martín-Banda et al., 2016, 2021). The Bajo Segura Basin is bordered to the south by a ENE-WSW-trending blind thrust fault (Fig. 1a): the Bajo Segura Fault (BSF; Alfaro et al., 2012; Alfaro et al., 2002).

Despite being a slow deformation region, both the historical seismic catalog (IGN-UPM, 2013) and evidence of Holocene paleo-earthquakes in several sites of the region (Ortuño et al., 2012; Martínez-Díaz et al., 2018; Masana et al., 2004; Ferrater et al., 2017; Insua-Arévalo et al., 2015; Martín-Banda et al., 2016) reveal that earthquake magnitudes greater than M_W 6.0 could be reached. In addition, depending on the

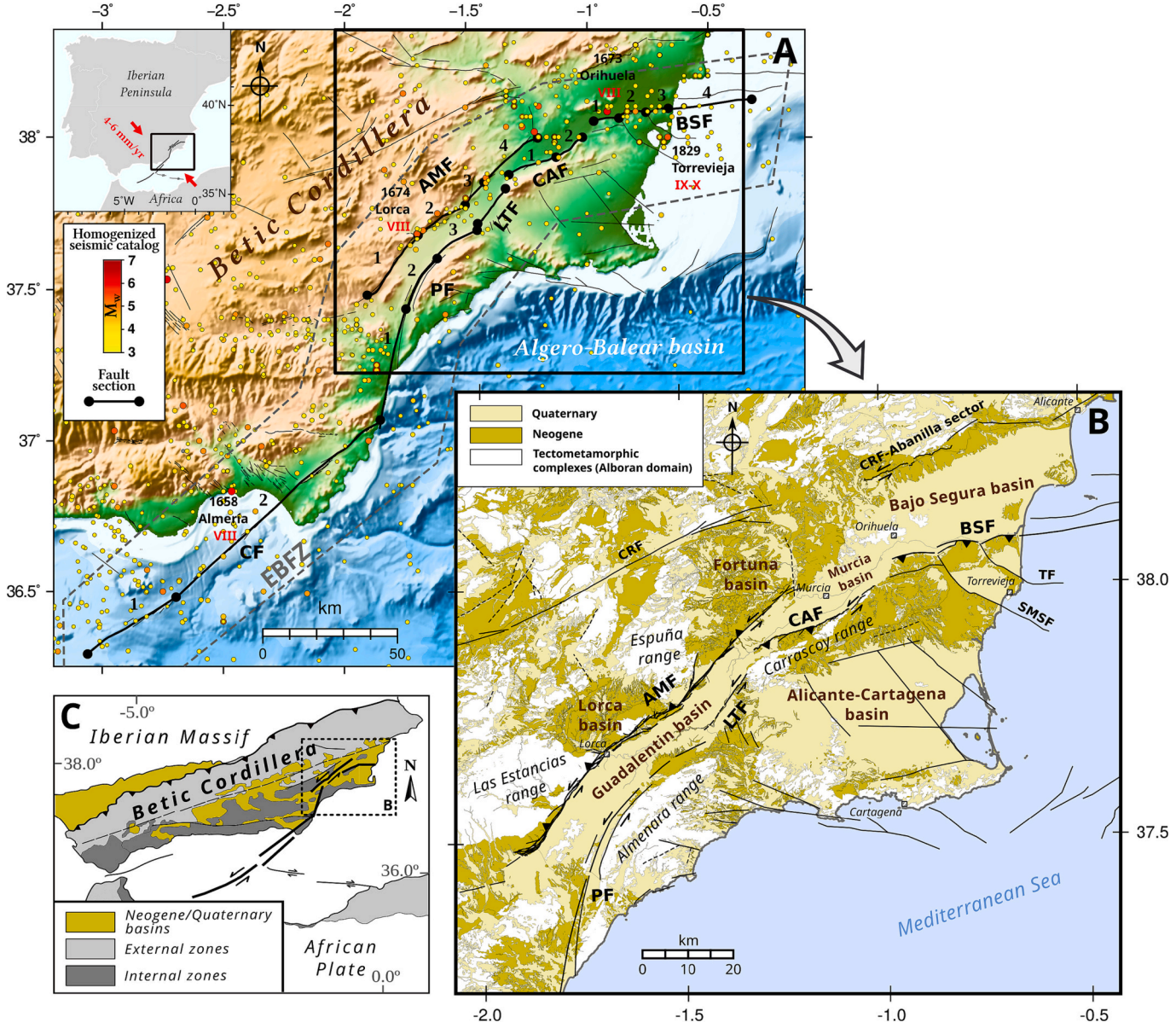

Fig. 1. a) Seismotectonic setting of the Eastern Betic Fault Zone (EBFZ). Seismicity data is from the homogenized earthquake catalog (IGN-UPM, 2013). The numbering of fault sections is based on the segmentation of the fault model proposed by Herrero-Barbero et al. (2021b). b) Geological map of the study region. Fault traces in black are taken from the Quaternary Active Fault Database of Iberia, QAFI v.3 (García-Fernández and Jiménez, 2012). These faults are: Carboneras fault (CF), Alhama de Murcia fault (AMF), Palomares fault (PF), Los Tollos fault (LTF), Carrascoy fault (CAF), Bajo-Segura fault (BSF), Crevillente Fault (CRF), San Miguel de las Salinas Fault (SMSF), and Torrevieja Fault (TF). c) Tectonic context of the EBSZ in the Betic Cordillera at the SE Iberia.

hypocenter depth, the complexity of the coseismic rupture (Martínez-Díaz et al., 2012a) and other site effects such as ground-motion amplification (Benito et al., 2007; Tsige and García Flórez, 2006) or near-fault directivity (Gordo-Monsó and Miranda, 2018), the seismic acceleration could be even greater than that described in the brief instrumental record. No observed strong motion data for moderate-large earthquakes is available besides the 2011, M_W 5.1 Lorca earthquake (maximum PGA 0.36 g). Consequently, the absence of large earthquakes in the instrumental catalogs and the lack of information about their possible rupture behavior hinder the estimation of the intensity of ground motions in the seismic hazard assessments in the EBFZ. Therefore, we wonder what could be the frequency of occurrence for large earthquakes almost without historical precedents in the EBFZ so far, and if the maximum earthquakes set in the hazard assessment should be reconsidered.

Besides the potential magnitudes reached, the intensity of ground shaking and the distribution of earthquake damage can be largely influenced by the nature of the geological deposits through the Eastern Betic region (Alfaro et al., 2001; García-Fernández and Jiménez, 2012; Tsige and García Flórez, 2006). Local site conditions strongly influence peak acceleration amplitudes and frequency content of surface motions (Seed et al., 1976; Semblat et al., 2005). The site amplification is controlled mainly by the geotechnical soil conditions (e.g., Aki, 1993; Borcherdt and Glassmoyer, 1992), and especially by their dynamic properties: shear-wave velocity, stiffness, damping, and relative density, among others (Wang and Hao, 2002). The amplification phenomenon related to soft soils or highly fractured materials was specially relevant in damaging earthquakes such as the 1985 and 2017 Mexico City (Cruz-Atienza et al., 2016; Franke et al., 2019); the 1989 Loma Prieta (Borcherdt and Glassmoyer, 1992); and the 2009 L'Aquila earthquakes (Ferraro et al., 2016), among others. According to these properties, the presence of thick and saturated soft soils, such as those that fill the Guadalentin and Bajo Segura Quatenary basins, generally determines the ground amplification and may increase the duration of the earthquake motion. Therefore, the integration of the site-dependent amplification, from a geothecnical- and geology-based approach (Borcherdt, 1994; Chen et al., 2021; Ramírez-Gaytan et al., 2020), into the hazard maps is key to determine the maximum ground accelerations.

We propose a deterministic seismic hazard analysis (e.g., Alonso-Henar et al., 2018; Anbazhagan and Abraham, 2020; Magrin et al., 2017) of large magnitude scenarios for the EBFZ. The main novelty of this study is obtaining maximum magnitudes through a physics-based numerical method, instead of using empirical relationships and statistical approaches (Anbazhagan et al., 2015; Kijko and Graham, 1998; Rivas-Medina et al., 2018). The latter methods are generally based on seismicity data that is limited in this slow deformation region. Our approach is based on the application of physics-based earthquake simulators (Rundle, 1988). Synthetic earthquake catalogs of thousands of years can be generated through efficient modeling of earthquake physics, emulating multiple seismic cycles and complex interactions between the faults of a system (Console et al., 2015; Robinson and Benites, 1995). The most recent numerical codes based on the rate- and state-dependent friction and sliding resistance (Dieterich, 1978; Ruina, 1983) allow the representation of the rupture process based on a quasi-dynamic approximation to the rupture nucleation and propagation (Richards-Dinger and Dieterich, 2012). These physics-based simulators have been applied in recent years in order to overcome the completeness limitations of the instrumental and historical seismic record in hazard studies (Álvarez-Gómez et al., 2023; Robinson et al., 2011; Shaw et al., 2018, 2022), also allowing the characterization of the behavior and frequencies of larger seismic ruptures (Herrero-Barbero et al., 2021b). In this paper, we will use the synthetic seismicity obtained with a physics-based earthquake simulator to define the magnitudes for earthquake-induced ground motion scenarios as a representation of the seismic threat in urban areas settled in the Guadalentin and Bajo Segura basins. Additionally, we will include the site dependent amplification through the geotechnical characterization of soils and rocks of the study area and the estimation of amplification factors.

2. Synthetic earthquake simulations

Due to the intrinsic characteristics of instrumental earthquake catalogs, and its limited time register compared to the long fault seismic cycles, the seismic hazard estimations are usually prone to uncertainties when dealing with major events. These uncertainties are higher in areas of low strain rate as the Betics. In order to overcome this limitation, we resort to a physics-based earthquake simulator, RSQSim (Richards-Dinger and Dieterich, 2012). RSQSim simulator is based on a boundary element formulation that integrates rate- and state-dependent friction (Dieterich, 1979; Ruina, 1983) and fault slip to generate long-term synthetic seismicity. Long-term stress interactions and earthquake slip are performed on each element of a fully-interacting 3D fault model following Okada (1992) elastic dislocation solutions. When the nucleation state is reached by a model element, the code computes the short-term rupture propagation to the neighboring elements through several approximations to rupture dynamics (see more details in Dieterich and Richards-Dinger, 2010, and Richards-Dinger and Dieterich, 2012), being still comparable (but more efficient) to those of fully dynamic codes. Therefore, earthquakes are spontaneously nucleated over the simulation time, reproducing an extensive synthetic record of earthquake ruptures with heterogeneous slip.

The 3D fault model that contains the geometry of the faults and the properties that define their kinematics is based on the Herrero-Barbero et al. (2021b) model. We base the simulations on the faults with the highest morphological expression and length in the EBFZ (Fig. 1a), including long-term slip rates and rakes of each fault section (Herrero-Barbero et al., 2021b). The model includes average values from multiple research done throughout the fault system (Alfaro et al., 2012; Alonso-Henar et al., 2020; Booth-Rea et al., 2004; Ferrater et al., 2017; Herrero-Barbero et al., 2020; Insua-Arévalo et al., 2015; Martín-Banda et al., 2016, 2021; Martínez-Díaz et al., 2012b; Moreno et al., 2015; Ortuño et al., 2012; Perea et al., 2012). We can assume that major earthquakes would be generated by some of these major faults, even though the absence of minor seismic sources in the model may influence the generation of a background small-magnitude seismicity (Herrero-Barbero et al., 2021b). Preference ranges of rate-and-state friction coefficients, which reproduce the effect of the velocity-change on the coefficient of friction (Dieterich, 1979; Ruina, 1983), are selected from experimental data obtained in the fault zone (Niemeijer and Vissers, 2014; Rodríguez-Escudero, E., 2017). Best-fit values of the input data that governs the simulation code were chosen through a testing process of multiple simulated catalogs varying the input parameters. This set of synthetic catalogs, as well as the input data used, are provided in the data repository of Herrero-Barbero et al. (2021a). We seek to match magnitude-frequency distributions with a Gutenberg-Richter b value close to 1.0 ± 0.1 (Fig. 2a) based on previous seismotectonic research on the same seismogenic zone (García-Mayordomo, 2005; IGN-UPM, 2013), magnitude-area empirical relationships (Fig. 2b), and the correlation between the synthetic seismicity with historical and paleoseismic data. Thus, the input model parameters of the best-fit synthetic catalog of 100,000 years are: rate-and-state friction parameters $a = 0.001$ and $b = 0.010$; a steady-state friction coefficient $\mu_0 = 0.6$; and a depth-variable normal stress with a 20 MPa/km gradient, with a resulting b-value of 1.05 (Fig. 2a). In Herrero-Barbero et al. (2021b), we observe a good agreement of the synthetic events with the annual occurrence rates for moderate-small earthquakes recorded in the IGN-UPM (2013) historical-instrumental catalog. As for the slip size, the synthetic seismicity better matches with the empirically observed trend for large earthquakes, as opposed to small-sized ones (Fig. 2b), which could be attributed to the finite grid dimensions (i.e., mesh resolution) leading to a saturation of slip (same behavior seen in Shaw et al., 2022) and/or to the homogeneous selection of friction parameters and initial stresses along the model. For the following analysis, we took only large

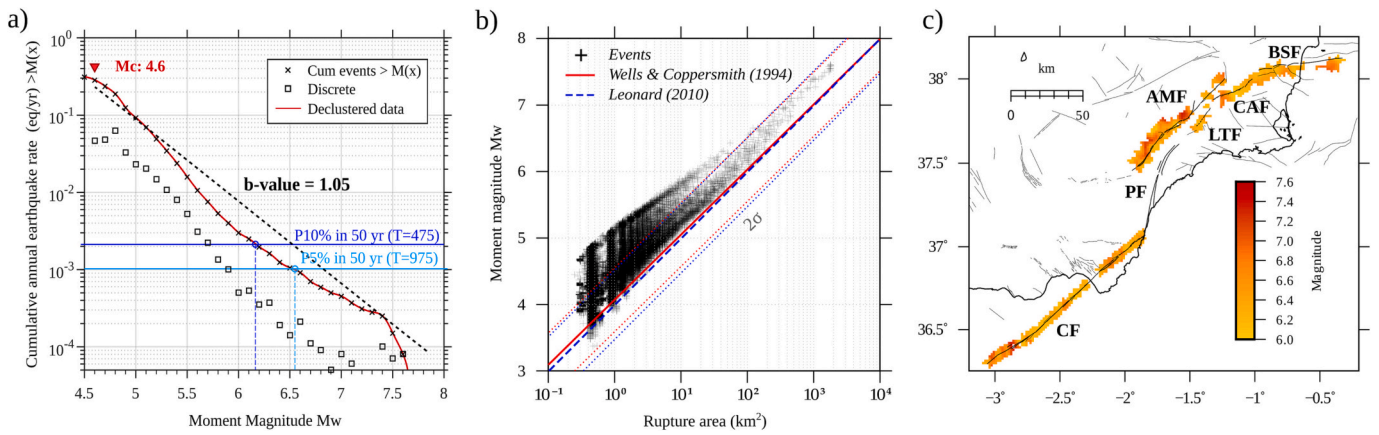

Fig. 2. Analysis of the best-fit synthetic earthquake catalog obtained using the RSQSim earthquake simulator code. a) Cumulative annual occurrence rate of events (R_i) *versus* the magnitude for the $M_W > 4.5$ events of the 100 ka synthetic catalog. The Gutenberg Richter b-value is calculated from an optimal magnitude of completeness M_C after a declustering procedure. The equivalent probabilities of excedeence of a magnitude $P[m \geq M]$ in 50 years (in terms of R_i, see Eq. (1)) are obtained from the declustered data. b) Magnitude-rupture area distribution of the synthetic seismicity against scaling relations (Leonard, 2010; Wells and Coppersmith, 1994). Dotted lines represent two standard deviations derived from the uncertainties of the regressions used. We observe that the Mw > 6 events are in a confidence area close to the scaling references. c) Spatial distribution of the $M_W > 6$ simulated events along the EBFZ model according to our RSQSim simulation.

magnitudes $M_W \geq 6.0$, which represent 0.5% of the seismicity simulated.

The multi-cycle earthquake simulations for this region shows that all modeled seismic sources could generate large $M_W > 6.0$ earthquakes in 100 kyr. Complete coseismic ruptures of the entire fault length are possible in the Alhama de Murcia fault (AMF), the Carboneras fault (CF), and the Carrascoy fault (CAF), just as large ruptures capable of re-nucleating on some nearby faults after an important static stress change (Herrero-Barbero et al., 2021b). Between the CF, located at the SW end of the EBFZ, and the Palomares Fault (PF), several branching ruptures would occur according to the simulation; while between the AMF and the Los Tollos Fault (LTF) we observed possible "jumping" coseismic ruptures by static stress transfer (Fig. 3a). The analysis of seismic threat in this research will focus on these large magnitudes and complex ruptures obtained in our earthquake simulations.

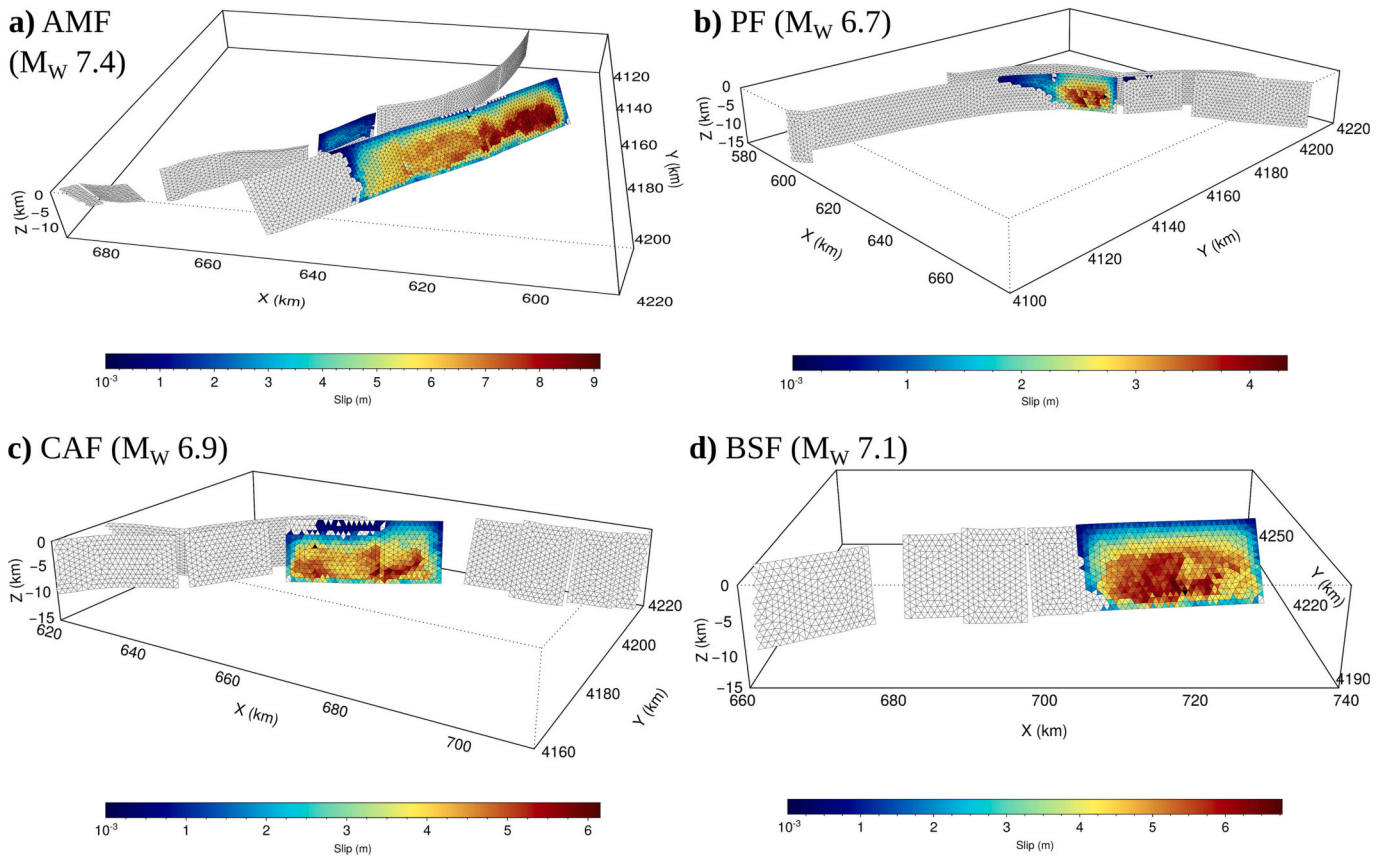

Fig. 3. 3D seismic ruptures of the maximum earthquakes obtained in the simulations with RSQSim. The range of values of heterogeneous slip is different in each representation of the colour scale.

2.1. Definition of seismic scenarios

From the synthetic seismicity model obtained, we propose some seismic scenarios in order to characterize the likely large ruptures originated in the most relevant seismic sources bounding the Guadalentin and Bajo Segura Quaternary basins. We will focus mainly on the AMF, the PF, the CAF and the BSF, due to their proximity to the urban areas located in the basins. Then, through a deterministic approximation, we have estimated the ground motion reached in those scenarios in terms of maximum peak ground acceleration, PGA (g).

Firstly, we selected the worst-case seismic scenarios of each fault source, analyzing the physical characteristics (hypocentral location, rupture area, style of faulting) of the events with the maximum magnitude in the 100 kyr synthetic catalog (Table 1). These parameters define the variables of the Ground Motion Prediction Equations (GMPE) that will be used to calculate the PGA on rock conditions (considering a shear wave velocity in the top 30 m of the site $Vs_{30} = 750$ m/s). The fault plane dimensions (projected XY coordinates) from which the distances to the seismic source are calculated, derive directly from the rupture surfaces simulated by the RSQSim code (Fig. 3). The GMPE assume an homogeneous slip distribution throughout the rupture area and only consider the rupture dimensions on the fault plane. In order to achieve a representative rupture from the maximum event, we selected the rupture area that represents the 95% of the total slip reached in each event (Table 1).

In addition to obtaining deterministic PGA scenarios based on maximum earthquakes, we also explored the ground motion associated with other specific magnitudes. These earthquakes match with an exposure time determined from synthetic seismicity (Fig. 2a), and are also closer to some historical magnitudes reached in the region, such as the M6.0 ± 0.8 Lorca earthquake in 1674, and the M6.6 ± 0.2 Torrevieja earthquake in 1829 (IGN-UPM, 2013). To do this, we selected the events from the catalog assuming an exponential Poisson model (Cornell, 1968) and calculating the probability of exceedance of a magnitude $P[m \geq M]$ in a period of t years:

$$P[m \geq M \text{in} t \text{years}] = 1 - e^{-R_i \times t,} \quad (1)$$

Given the long catalog duration and the high number of events of the synthetic seismicity model that we present, we assume: a cumulative annual occurrence rate of events, R_i; a reference time t of 50 years equivalent to the minimum time exposure considered for ordinary buildings; and the exceedance probabilities of 5 and 10% (Fig. 2a). In our synthetic earthquake catalog, magnitudes corresponding to a probability of 10% in 50 years are equivalent to the magnitudes M_W 6.1–6.2, while the probability of exceedance of 5% in 50 years would correspond to magnitudes M_W 6.5–6.6. At this point, we emphasize that we are not referring to probabilities of exceedance of the level of movement, as the probabilistic hazard studies strictly do, but rather evaluating the probability of exceedance of a certain magnitude within the synthetic 100 kyr earthquake catalog. In this case, we selected magnitudes from the Alhama de Murcia and Bajo Segura faults to elaborate the PGA scenarios, taking the rupture dimensions by means of the previously described procedure.

2.2. Selection of GMPE models

One of the critical points of ground-motion estimation, whether from a deterministic or probabilistic approach, is the assignment of the GMPE. This paper deals with the implication of infrequent large magnitude earthquakes ($M_W > 6$), for which there is no instrumental record of accelerations in the region that can be used to calibrate the GMPE. This makes it very difficult to choose an equation or assign weights to a set of models. In this work, we use the European model of Akkar et al. (2014) (AKK14). AKK14 presents a wide range of applicability of magnitudes ($4.0 < M_W < 7.6$) and distances ($R < 200$ km); and includes input parameters that consider rupture geometry and fault kinematics. In recent years, numerous hazard assessments have incorporated this equation among their prediction models used (e.g., Aochi et al., 2017; Gómez-Novell et al., 2020; Valentini et al., 2017). In our analysis, AKK14 equations have been implemented for the calculation and realization of maps with the GMT software (Wessel et al., 2013).

The common practice in hazard studies is the selection of a set of GMPE to consider epistemic uncertainties. However, a single attenuation equation has been used here to facilitate the analysis of the implications on regional seismic hazard of the synthetic seismicity obtained. Since it is a deterministic approach, multiple scenarios are reproduced and the use of several GMPE would make it harder to compare. To calibrate the sensitivity of the AKK14 model in the results obtained (magnitudes, geometries, kinematics, and slip rates), some of the scenarios have been computed also with the GMPE proposed by Campbell and Bozorgnia (2014) (CB14) under rock conditions ($Vs_{30} = 750$ m/s). The CB14 model is based on global databases from the Next Generation Attenuation (NGA) Project, and adds some components to the equation related to hypocentral depth and fault dip that are not included in AKK14. This equation has previously been used for seismic hazard studies in the EBFZ (Gómez-Novell et al., 2020; Rivas-Medina et al., 2018). Due to the numerous components of this formulation, OpenSHA software (Open-Source Seismic Hazard Analysis; Field et al., 2003) has been used for calculations with CB14, which allows us to solve multiple types of distance measurements. The realization of the PGA maps and curves has been done again with GMT (Wessel et al., 2013).

3. Evaluation of the site-dependent response

In order to evaluate the site-dependent amplification of the ground motion during a possible large earthquake, the geothecnical

Table 1
On the left, the characteristics of the maximum events obtained in the 100 ka earthquake simulations for the four analyzed seismic sources.

Maximum Events obtained in the Simulations					Fault source input parameters			
M_{max}	Fault	Epicentral section	Rupture area (km^2)	Annual frequency in 100 kyr (events/yr)	Dip (°)	Rake (°) (Main style of faulting)	Mean Slip rate (mm/yr) of the section [uncertainty]	References
7.4	Alhama de Murcia Fault	AMF-2	1004.11	8×10^{-5}	55–65	39 (Strike-slip)	0.9 [0.80–1.00]	Ferrater et al. (2017); Martínez-Díaz et al. (2012a); Alonso-Henar et al. (2020)
7.1	Bajo Segura Fault	BSF-4	403.20	1×10^{-5}	45–50	90 (Reverse)	0.15 [0.15–0.25]	Alfaro et al. (2012); Perea et al. (2012)
6.9	Carrascoy Fault	CAF-1	344.47	4×10^{-5}	85	15 (Strike-slip)	0.37 [0.29–0.45]	Martín-Banda et al. (2016)
6.7	Palomares Fault	PF-3	213.48	1×10^{-5}	75	15 (Strike-slip)	0.10 [0.04–0.16]	Inferred from PF-2: Booth-Rea et al. (2004).

On the right, the geometric and kinematic data used in the Herrero-Barbero et al. (2021b) fault model, corresponding to the fault sections where the maximum earthquakes are nucleated (epicentral section). The main style of faulting, the mean dip and the rakes have also been used as input parameters in the GMPE (Akkar et al., 2014; Campbell and Bozorgnia, 2014) for the analyzed seismic scenarios.

classification of the site materials constitutes the first fundamental step. There are obvious difficulties in obtaining in-situ geological data at very large regional areas (as in this study of the Eastern Betics). To overcome this limitation we resort to the classification of surface geological materials into categories with similar seismic response (e.g., Borcherdt, 1994; Chen et al., 2021; Dobry et al., 2000; Ramírez-Gaytan et al., 2020; Street et al., 1997) to later attribute amplification factors to them, using local and international codes. These studies and international standards assume intervals of shear-wave velocity based on the geotechnical characteristics of the near-surface geological formations (Vs_{30}) and empirically correlate other dynamic soil properties. We have used various criteria based on the soil classification of Borcherdt (1994) and the American standard (National Earthquake Hazards Reduction Program, NEHRP; BSSC, 2015, 2020), starting from the zonification of the Murcia region based on site-dependent response by Tsige and García Flórez (2006). The aforementioned studies allow us to infer representative values, not only for geomechanical properties, but other characteristics that influence the seismic response of the ground, such as plasticity, saturation degree of soils, the thickness of soft soil layering, and hence the impedance ratio between sediments and bedrock.

For the classification of soils and rocks in the area, numerous available geological and geotechnical information has been examined:

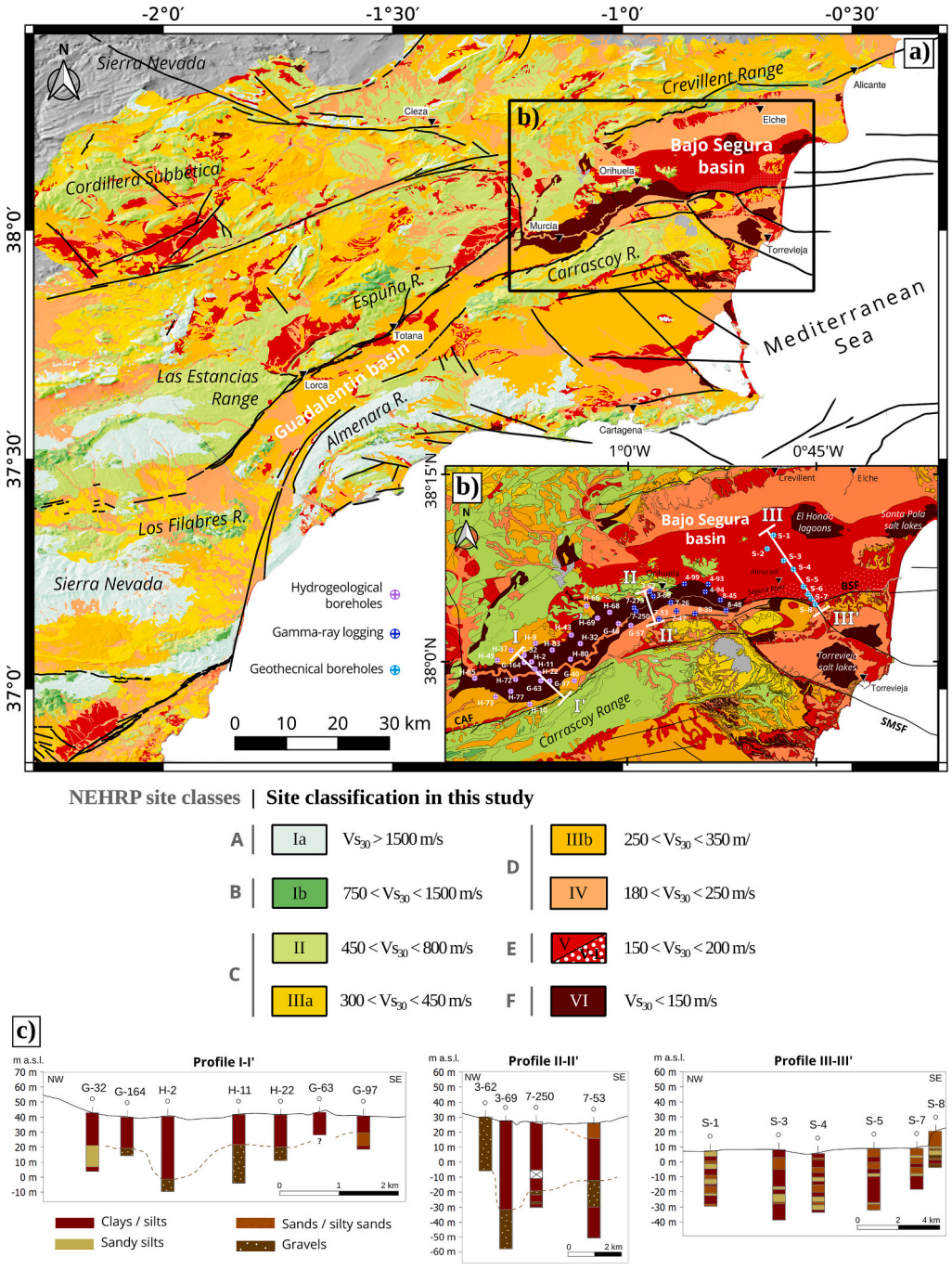

Fig. 4. a) Geotechnical classification of near-surface soils and rocks of the study region. a) Regional map of the 8 geotechnical site categories classified in Table 2 according to ranges of shear-wave velocities Vs_{30}. The correlation of our classification with the NEHRP site classes (BSSC, 2015) is also shown. b) Detailed soils map of the northern end of the Guadalentin depression and the Bajo Segura basin, with locations of boreholes consulted in the geotechnical analysis (Delgado, 1997; IGME, 2000; Tomás-Jover, 2009). c) Cross-sections of representative borehole logs projected, with the thickness of the soils represented in b).

regional and local geotechnical maps (IGME, 1973, 1977, 1984); in-situ test data (Alfaro et al., 2001; Delgado, 1997); and geotechnical and hydrogeological borehole data (Fig. 4c; Delgado, 1997; IGME, 2000; Tomás-Jover, 2009). Furthermore, some local in-situ shear-wave velocity (Vs) data have been reviewed in order to validate our classification based on geological and some geotechnical data (Table 2). In the Bajo Segura basin, Rosa-Cintas et al. (2011) and García-Fernández and Jiménez (2012) characterize the sediments in the Segura river floodplain and the Hondo and Santa Pola lagoons (Fig. 4b), estimating values of Vs < 220 m/s for clay soils of 50 m thick, which are agree with our Class V (150–200 m/s; Table 2). Delgado et al. (2003) estimate the relative density of soils in the S-SE of the Bajo Segura Basin, obtaining SPT values of N_{SPT} < 10 in most of clay and soft silt deposits. No empirical relations between Vs and N-SPT have been estimated for the soils of our study area, but we can correlate the minimum values $N_{SPT} = 5 \pm 3$ of Delgado et al. (2003) according to other relations for comparable soil characteristics: Vs = 125 ± 25 m/s for clays (Imai, 1977), Vs = 156 ± 39 m/s for silts (Tsiambaos and Sabatakakis, 2011), Vs = 105 ± 27 m/s for similar Quaternary alluvial soils (Dikmen, 2009); and a Vs = 137 ± 47 m/s for high plasticity clays in another region of Spain but with different age (Pérez-Santisteban et al., 2016). Tsige and García Flórez (2006) also estimated similar values of Vs < 130 m/s for special soils (muds, clays and soft silts) of the Guadalentín basin (Fig. 4b) through the Imai (1977) correlation. Therefore, the soils in the Bajo Segura basin were zoned as Class VI (<150 m/s) in our classification.

We classified the geological formations of the study region into 6 categories based on their geotechnical properties and V_S values (Fig. 4a and Table 2). After, we correlate our classification with the soil classes defined by BSSC (2015) to assign an amplification factor, as shown in Fig. 4. In the Table S1 of the Supplementary Material, it is provided an extension of Table 2 that compares our geothecnical classification with the classifications of Borcherdt (1994) and BSSC (2015, 2020). From a geotechnical point of view, the large lithological variability exhibited in the study area results in site classes with different mechanical strengths (Fig. 4a): from hard and competent rocks (i.e., Paleozoic metamorphic rocks, Triassic carbonates, sandstones and Miocene calcarenites) to very soft, sensitive and even saturated soils (classes V and VI; Table 2) from the recent Quaternary Bajo Segura basin and northern end of the Guadalentin basin (Fig. 4b). The latter soils deserve special interest due to their geotechnical properties, thickness, liquefaction susceptibility, and could lead to a considerable increase in ground motion during an earthquake. Rocks of medium-low resistance, hard soils and Quaternary unconsolidated soils that mainly form the Tertiary basins and the southern half of the Guadalentin depression also deserve attention, since they represent a moderate-high susceptibility to site amplification (classes IIIb and IV; Table 2).

Table 2
Geotechnical classification based on the near-surface geological materials of the Eastern Betics.

Classification criteria		Site class		
Lithology description	Geotechnical description	This Study	Shear-wave velocity Vs_{30} (m/s) interval	*NEHRP* 2015 classes Vs_{30} (m/s) interval
• **Paleozoic medium-high grade metamorphic rocks** (e.g., quartzite, quartzite schists and little-altered gneisses); **dolomites;** and **massive facies of igneous rocks without hydrothermal alteration** (e.g. lamproites and diabases of Murcia and Alicante).	Very hard rocks, with few or no fractures.	I.a.	> 1500	A > 1500
• **Low grade metamorphic rocks** (phyllites) interspersed with quartzites; **dolomite and limestone** intercalations; and **consolidated sandstones and calcarenites** (Upper Cretaceous-Tertiary) with occasional conglomerates.	Hard rocks with very widely spaced fractures. Intercalation of very hard and hard rocks.	I.b.	750–1500	B 760–1500
• **Limestones**, frequently accompanied by calcarenites and/or sandstones; **cemented pre-Tertiary conglomerates** with sandstones and carbonates; fractured dolomites with marly levels; and locally, altered slates and **graphite-bearing mica schists**.	Firm to hard rocks, very fractured and/or with intercalations of soft rock layers.	II	450–800	C 360–760
• **Marls** and limestone-marl alternations, with occasional gypsum (Miocene); travertines and recent tobaceous and reef limestones; shale-marl alternations; and Upper Miocene sandstones and marls (turbiditic systems).	Soft to firm rocks, very fractured. Abundant intercalations of soft rocks and stiff soils.	III.a.	300–450	
• **Triassic variegated clays, marls and gypsum** from Keuper facies; **clays and sands** from Weald facies in the External Prebetic (Cretaceous Inf.). • **Miocene-Pliocene sedimentary rocks and sediments** (e.g., turbiditic sandstones with clays and sands; conglomerates with silts and sands; fluvio-lacustrine limestones; and **massive volcanic rocks (domes and dikes) with intense hydrothermal alteration**. • **Holocene caliches, calcareous stiff soils**, and crusted glacis.	Soft rocks with expansive clays, >30 m thick. Poorly cemented non-cohesive soils, >10 m thick.	III.b.	250–350	D 180–360
• **Quaternary alluvial-fluvial sediments** (terraces, fans, channels), coastal sediments (terraces, wave-cut platforms) and debris-flow deposits (e.g. blocks, pebbles, gravels and sands). Middle-Upper Miocene **pyroclastic breccias**.	Non-cohesive gravelly soils. Dense sands and stiff to hard clays (N > 5 blows/ft).	IV	180–250	
• Fluvial and fluvio-lacustrine sediments, and coastal and wind-deposited sediments (beaches, dunes, littoral bars and estuaries): **very soft to soft clays, silty clays and sands**. • **Expansive soil deposits** of diatomaceous marls; and **lapilli tuffs and ignimbrites with clay minerals from hydrothermal alteration (bentonites)**.	Soft cohesive soils (PI >20, N < 5 blows/ft). Non-cohesive loose soils, more then 10 m thick.	V	150–200	E < 180 (150–180)
• Quaternary fluvial sediments **with high organic matter: silts and organic clays**. Marshlands, salt lakes, coastal lagoon and endorheic deposits: **peat soils, muds, organic silts, sands and hydromorphic soils**.	Very soft soils, >3 m thick. Saturated soils (water table <10 m deep). High plasticity (PI >75) and sensitive clays. Liquefiable soils.	VI	< 150	F < 150 (100–150)

The lithologies in **bold** are the most abundant on a regional scale.

Table 3
Site amplification factors F_{PGA} taken from ASCE (2017) based on the site classes defined by the BSSC (2015) recommendations.

Site class	Vs_{30} (m/s)	PGA ≤ 0.1	PGA = 0.2	PGA = 0.3	PGA = 0.4	PGA = 0.5	PGA ≥ 0.6
A	$Vs_{30} > 1500$	0.8	0.8	0.8	0.8	0.8	0.8
B	$760 < Vs_{30} < 1500$	0.9	0.9	0.9	0.9	0.9	0.9
C	$360 < Vs_{30} < 760$	1.3	1.2	1.2	1.2	1.2	1.2
D	$180 < Vs_{30} < 360$	1.6	1.4	1.3	1.2	1.1	1.1
E	$Vs_{30} < 180$ *(150 < Vs_{30} < 180)*	2.4	1.9	1.6	1.4	1.2	1.1
*F**	$Vs_{30} < 150$ *(100 < Vs_{30} < 150)*	*2.6*	*1.9*	*1.6*	*1.4*	*1.2*	*1.1*

Factors for intermediate values of PGA on rock are calculated by straigth-line interpolation.

3.1. Soil amplification factors

To assign site-dependent amplification factors to the GMPE, we have chosen the classification criteria provided by BSSC (2015). Based on these soil classes, the American seismic design code ASCE / SEI Standard 7–16 (ASCE, 2017) assigns amplification factors depending on the input PGA (Table 3), so that:

$$PGA_M = F_{PGA} \times PGA_{REF}, \quad (2)$$

where PGA_M is the maximum peak ground acceleration adjusted for site class response, F_{PGA} is the amplification factor, and PGA_{REF} is the input peak ground acceleration calculated using the AKK14 equation for standard hard rock conditions (750 m/s) with no amplification. The amplification factors defined by ASCE (2017) are widely used for the seismic design, but it has also been applied in several publications on site effect characterization (e.g., Alonso-Henar et al., 2018; Benito et al., 2007; Chen et al., 2021; Ramírez-Gaytan et al., 2020). Class F soils are defined by BSSC (2015) as particularly vulnerable special soils, with values of $Vs_{30} < 180$ m/s, like Class E but requiring a specific analysis. In this work, we constrained a range of Vs_{30} values for Class F ($100 < Vs_{30} < 150$ m/s); and through the regressions provided by ASCE (2017) from empirical data and numerical simulations (Dobry et al., 2000; Stewart and Seyhan, 2013), we calculated an amplification coefficient of $F_{PGA} = 2.6$ for an input PGA ≤ 0.1 g (Table 3). For the rest of input values of PGA_{REF}, we selected the same coefficient with respect to Class E. Note that the ASCE (2017) factors already include a conservative margin of error (Table 3), since at higher acceleration levels ($PGA_{REF} \geq 0.2$ g) the nonlinearity of soft soils could prevent them from reaching higher PGA values than those observed on rock (i.e., deamplification) (Wen et al., 1994).

Therefore, soil amplification in this region has been calculated and transformed into a raster map with a resolution of 500 m/pixel (Fig. S1 of the Supplementary Material), and then incorporated to the PGA scenarios estimated on rock using AKK14 to consider soil amplification in the resulting calculations.

4. Seismic hazard scenarios of PGA

We present deterministic PGA scenarios for 4 major faults of the EBFZ. Two of these faults, the Alhama de Murcia (AMF) and the Palomares fault (PF), border the Guadalentin basin, while the Bajo Segura fault (BSF) limits the Bajo Segura basin to the south. Among them, the Carrascoy fault (CAF) delimits the northeastern end of the Guadalentin basin, where the city of Murcia is located (Fig. 1b).

A maximum simulated earthquake in the AMF from our synthetic catalog (Fig. 3a) is a magnitude M_W 7.4 (M_0 = 1.5e+20 Nm) complex event nucleated in the Lorca-Totana fault section (AMF-2; Fig. 1a), near the town of Lorca. According to the detailed slip record obtained, the rupture propagates along three of the fault segments until ceasing and re-nucleating in the nearby Los Tollos fault (Fig. 3a) through static stress transfer. Regarding the ground motion measures by AKK14 for this complex rupture in the AMF, the PGA (g) values on rock would slightly exceed 0.5 g (Fig. S2a in Supplementary Material). The latter could be amplified above 0.6 g in the NW hanging-wall of the fault (Fig. 5a), where soft rocks from the Miocene basins are abundant. This event would generate the largest regional extension of ground motion for site-dependent PGA > 0.1 g, reaching moderate accelerations in some further areas at the south of the Guadalentin valley. Maximum accelerations close to the source also cover a considerably greater area than in other scenarios, due to the 'jumping' rupture and the dipping geometry of the AMF (Fig. 5a). Urban areas located along the Guadalentin basin (e.g., Lorca and Totana, on the fault trace) could be subject to PGA values around 0.59 ± 0.03 g (Fig. 5c). Likewise, the worst-case scenario simulated in the PF (M_W 6.7, M_0 = 1.38e+19 Nm) would exceed a PGA of 0.5 g in the first 5 km close to the source, affecting the southern half of the Quaternary basin (Fig. 5b). In this case, the PGA at Lorca town reaches a PGA of 0.31 ± 0.05 g (Fig. 5d).

The populated city of Murcia also reaches values higher than 0.3 g in the AMF scenario despite the distance (0.33 ± 0.01 g; Fig. 5c). This indicates a strong influence of soil-dependent response in the northern Guadalentin basin for maximum synthetic earthquakes nucleated in its bounding seismic sources. This includes the worst-case scenario of the CAF: a maximum M_W 6.9 earthquake (M_0 = 3.4e+19) with hypocenter in the SW section (CAF-1, Fig. 1a). This rupture could cover the entire surface of the CAF, according to the synthetic model (Fig. 3c). The ground motion scenario (Fig. 6a) shows a maximum PGA close to 0.6 g reached on the fault trace, where some urban areas are located. The thick and very soft deposits (Class F soils) at the north of the Guadalentin depression (Fig. 4b) contribute to exceeding PGA values of 0.5 g, which could signify a severe damage in the city of Murcia (Figura 6c). Moreover, the entire Bajo Segura basin would be subject to PGA > 0.2 g (~0.42 ± 0.03 g in the town of Orihuela; Fig. 6c). There, an important

site amplification at the south of Bajo Segura basin is probably due to very soft and saturated clays from the Quaternary alluvial plain (Fig. 4b). The incidence in this area would be considerably higher in the case of the maximum synthetic earthquake in the BSF: a M_W 7.1 event (M_0 = 3.4e+19 Nm) whose rupture area is propagated along the offshore section (Fig. 3d), which is the largest segment mapped in the Bajo Segura fault zone (Alfaro et al., 2012; Perea et al., 2012). However, the rupture is not transferred to nearby sections, so the greatest earthquake-induced ground motion (PGA ~0.6 g) would affect the coastline between the densely populated areas between Torrevieja and Santa Pola (Fig. 6b). On the soft clay soils near the Segura river, around a PGA = 0.5 g is reached, which are considerably greater than those estimated on rock conditions (Fig. S2d of the Supplementary Material).

We have also explored other synthetic earthquake scenarios that, although not being the worst cases in a period of 100 kyr, could imply an important threat in some critical zones of the region for shorter exposure times. In this case, we have selected seismic sources located in the areas with highest frequent of simulated seismicity and higher magnitudes on the northern side of the EBFZ (Fig. 2c): the southern sections of the AMF and the BSF. Some historical events with macroseismic intensities of $I_{EMS} \geq$ VII (Fig. 1a) are associated to these areas, whose moment magnitudes are estimated to be greater than M_W 6. Thus, we generate representative scenarios for a magnitude between M_W 6.1–6.2, corresponding to a probability of 10% in 50 years; and an event of M_W 6.5–6.6, equivalent to the probability of exceedance of 5% in 50 years for the resulting synthetic catalog. For each scenario, a representative event has been taken among the most frequent obtained in the simulation for the selected range of magnitudes (white stars in Fig. 7).

In the AMF scenario for a magnitude M_W 6.2 (Fig. 7a), the rupture would break partially the southern section (AMF-1 or Góñar-Lorca section) plane, which would have a significant impact on urban areas and infrastructures located south of the Guadalentin basin: for example, Puerto Lumbreras (PGA = 0.420 ± 0.005 g) and Lorca (PGA = 0.36 ± 0.03 g). For a magnitude M_W 6.6 (Fig. 7b), the representative rupture area covers almost the entire length of the two southern fault sections, extending the largest values of PGA to the towns of Góñar and Totana. At Lorca town, located next to the epicenter, a PGA of 0.51 ± 0.01 g is estimated.

Although the highest rupture probability obtained is in the offshore section, the BSF scenarios selected (Fig. 7c,d) are representative of the most frequent simulated onshore ruptures. The rupture area selected for the BSF covers around the 50% of the Hurchillo section surface (BSF-1)

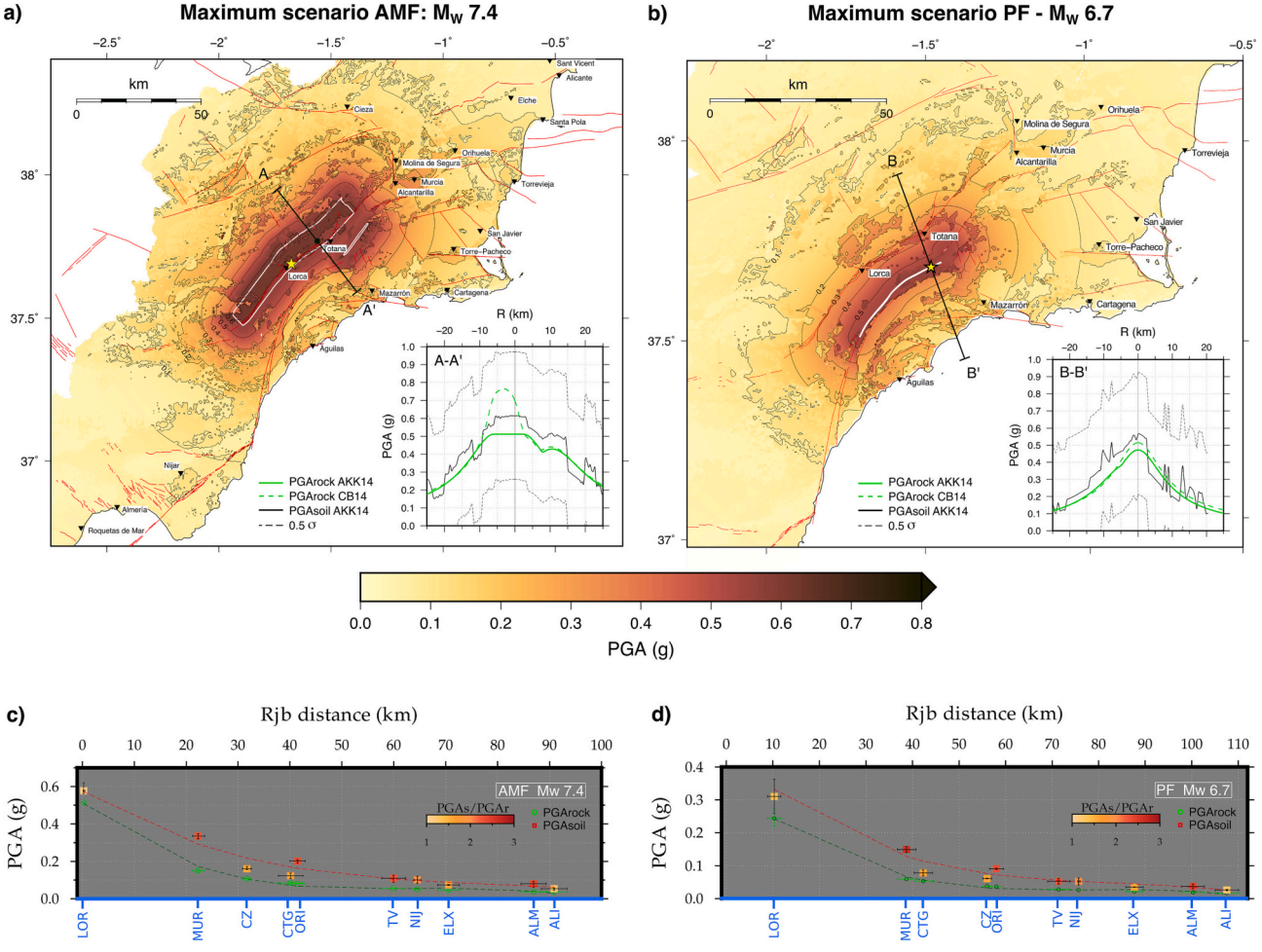

Fig. 5. Worst-case PGA (g) scenarios for a) the Alhama de Murcia Fault (AMF), and b) the Palomares Fault (PF), estimated using the GMPE of Akkar et al. (2014). In the lower right corner, PGA distribution calculated with Akkar et al. (2014) and Campbell and Bozorgnia (2014) equations, as a function of horizontal distance to the fault trace projected over a 50 km transverse transect. PGA estimated under rock conditions is shown in green and the site-effect PGA curve (PGA_{soil} here; PGA_M in Eq. (2)) is shown in black, with the uncertainty as a dashed line. The sites where the black curve is below the green curve are related to rock massifs. The yellow star represents the epicenter of the synthetic event. c) and d) show the estimations of PGA reached in towns of the Eastern Betics with >30 k inhabitants in the simulated maximum events. We represent the average value with its uncertainty within a buffer diameter of up to 5 km around the town center. In green, we show the estimated PGA on rock, and in warm colors, those obtained considering the site amplification, from null amplification (PGAsoil/PGArock = 1) to 3 times the value of PGArock. The towns are, from south to north: Níjar (NIJ), Almería (ALM), Lorca (LOR), Cartagena (CTG), Murcia (MUR), Cieza (CZ), Orihuela (ORI), Torrevieja (TV), Elche (ELX) and Alicante (ALI). (For interpretation of the references to colour in this figure legend, the reader is referred to the web version of this article.)

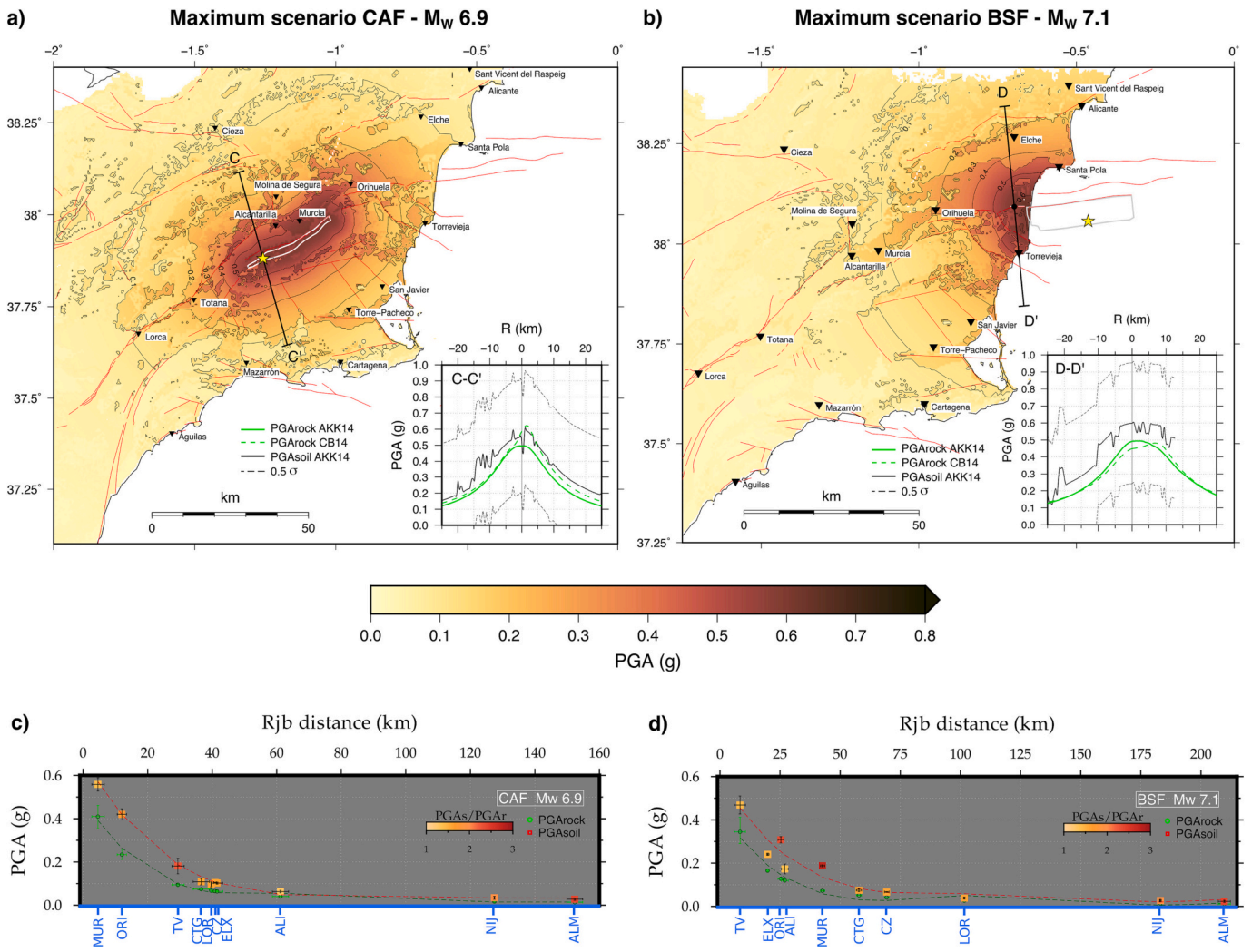

Fig. 6. Worst-case PGA (g) scenarios for a) the Carrascoy Fault (CAF), and b) the Bajo Segura Fault (BSF), estimated using the GMPE of Akkar et al. (2014). In the lower right corner, PGA distribution calculated with Akkar et al. (2014) and Campbell and Bozorgnia (2014) equations, as a function of horizontal distance to the fault trace projected over a 50 km transverse transect. PGA estimated under rock conditions is shown in green and the site-effect PGA curve is shown in black, with the uncertainty as a dashed line. The yellow star represents the epicenter of the synthetic event. c) and d) show the average estimations of PGA reached in towns at the SE Spain with >30 k inhabitants for the simulated maximum magnitudes. The procedure, legend and labels of the towns are the same as the Fig. 5. (For interpretation of the references to colour in this figure legend, the reader is referred to the web version of this article.)

for a magnitude M_W 6.2 (Fig. 7c), and the entire surface of the section for a magnitude M_W 6.6 (Fig. 7d). As in the worst-case scenarios, the south Bajo Segura basin and the Torrevieja coastline are the regions where the most severe accelerations would be reached for $M_W > 6$ synthetic earthquake scenarios. The PGA reached in numerous nearby urban areas would exceed the value of 0.5 g, highlighting the populated town of Orihuela: 0.50 ± 0.01 g in Fig. 7c and 0.57 ± 0.01 g in Fig. 7d.

5. Discussion

5.1. Implications of the synthetic rupture model in the scenarios

The maximum scenarios estimated in this study are based on a 3D model of the main seismogenic sources of the EBFZ. Although our deterministic analysis focuses on the faults that limit the Quaternary basins, the interactions of the latter with the rest of faults must be taken into account in the synthetic seismicity model obtained through the RSQSim earthquake simulations. The maximum earthquakes reached in the 100 kyr simulation and, therefore, the peak ground accelerations resulting from these events, depend largely on the input parameters established for these faults (Table 1). Earthquake recurrence are mainly controlled by the input slip rates and complex geometries (Dieterich and Richards-Dinger, 2010; Milner et al., 2022), whereas the earthquake size and energy released are a consequence of the rupture area and the co-seismic slip generated, which, in turn, also depend on the frictional properties, stress conditions and fault geometries (lengths, seismogenic depths) set in the simulations (Herrero-Barbero et al., 2021b; Oglesby, 2008; Shaw, 2019; Wollherr et al., 2019).

The maximum synthetic earthquake nucleated in the populated areas located around the Guadalentin depression correspond to one of the southern sections of the AMF (Table 1) with high average slip rate (Ferrater et al., 2017). Our multi-cycle simulations show that a maximum M_W 7.4 event is generated up to 8 times throughout the 100 kyr simulation (Table 1), but with disparate inter-event times between 7000 and 27,000 years. This recurrence variability observed in the synthetic seismicity reflects the influence of stress interaction in a multi-fault system, and suggests not ruling out a possible underestimation of the seismogenic potential of a fault during a long time period without major events. According to the ground motion estimation from the empirical prediction model of AKK14 incorporating the site-dependent effect, a PGA value above 0.6 g would be reached on the source (Fig. 5a). As the AKK14 model uses a horizontal distance (Rjb) to the

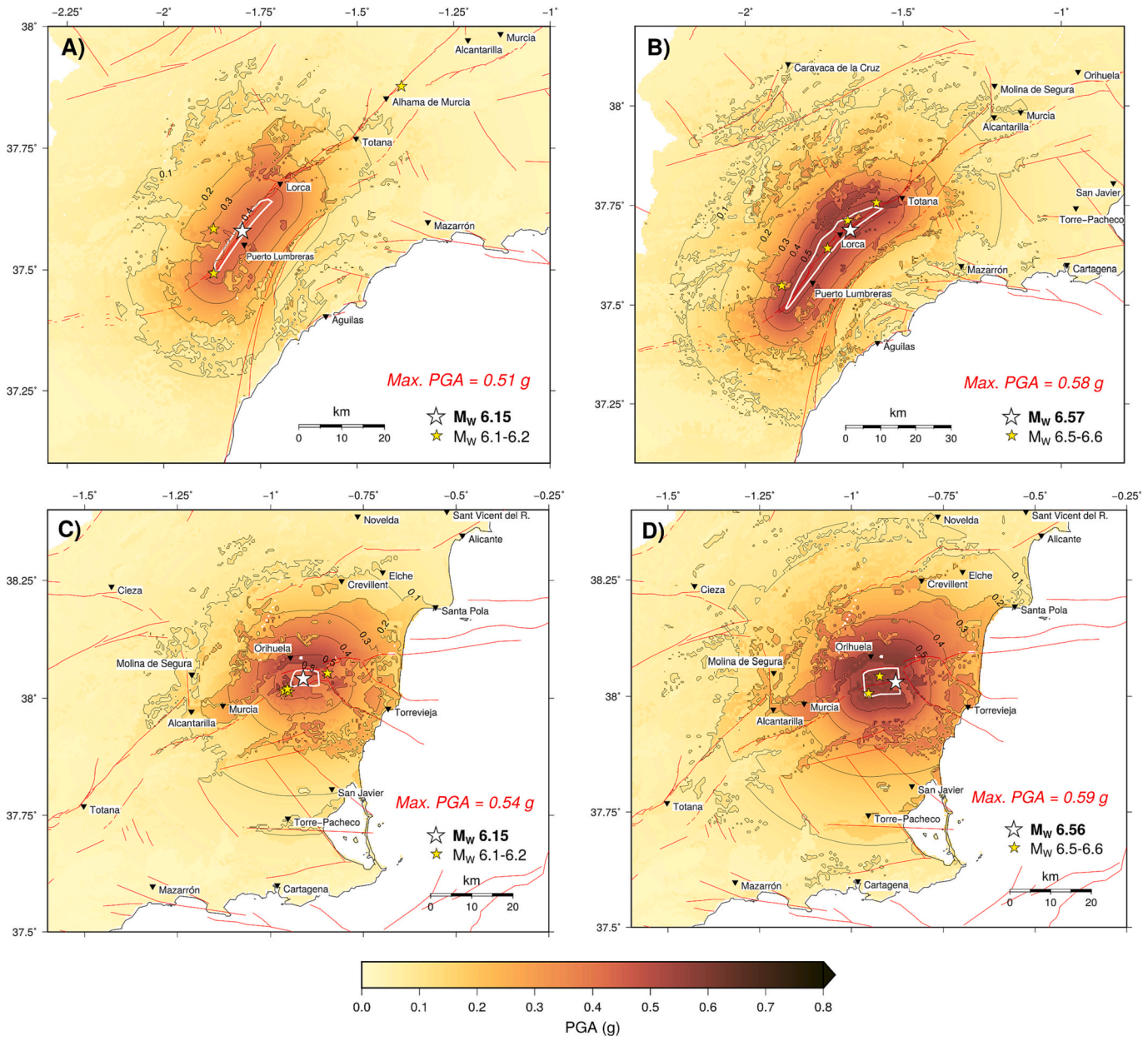

Fig. 7. PGA (g) scenarios for given probabilities of exceedance of a magnitude in a certain period of time, assuming that the synthetic earthquake catalog obtained fully represents the seismicity of the region. Representative events nucleated in the Alhama de Murcia (AMF) and Bajo Segura (BSF) faults have been selected. a) and c) PGA (g) scenarios with soil amplification for magnitudes M_W 6.1–6.2, corresponding to a probability of exceedance of 10% in 50 years. b) and d) PGA scenarios (g) with soil amplification for magnitudes M_W 6.5–6.6, corresponding to a probability of exceedance of 5% in 50 years.

surface projection of the rupture (Joyner and Boore, 1981), the distribution measured along the A-A' transect (Fig. 5a, bottom right plot) shows a plateau shape not observed in other subvertical faults, such as the PF (B-B′ transect; Fig. 5b). CB14 model, however, includes a hanging wall function with the closest distance resulting in a larger PGA > 0.75 g in the fault plane projection region (Figs. 5a and 8a), which is remarkable in terms of hazard distribution.

Regarding the simulated maximum earthquake in the Bajo Segura basin, we found a M_W 7.1 earthquake in the offshore section of the Bajo Segura Fault. Only one earthquake of this magnitude is reached in 100 kyr of simulation, while magnitudes M_W 6.5–6.6 events (similar to the estimations for the 1829 Torrevieja earthquake) are generated up to 4 times in the same time interval. Analyzing the scenarios for exposure times of <100 kyr based on the frequency of simulated events (Fig. 7), we observe that the onshore sections of the BSF also concentrate this significant activity due to their moderate slip rates (e.g., 0.40 ± 0.11 mm/a in the Hurchillo segment; Alfaro et al., 2012). The BSF has been modeled with a reverse kinematics that tends to limit the rupture propagation laterally to adjacent sections and faults (Herrero-Barbero et al., 2021b). Furthermore, its 45–50° fault dip (Perea et al., 2012) seems to induce a greater extension of the highest PGA on the hanging wall, as observed in the scenarios on rock conditions (Figs. S2d and S3d of the Supplementary Material), although this effect is more diffuse when we add the site amplification due to the very soft and thick soils located in the footwall (Fig. 7d). Consequently, fault geometry combined with site-dependent amplification for magnitudes M_W 6.5–6.6 (5% probability of exceedance in 50 years) conditions PGA values >0.5 g reached near the source, affecting a ~ 400 km^2 area where many highly populated towns, such as Orihuela, are located.

We have also represented co-seismic ruptures resulting from the slip

transfer to nearby or parallel sections of the fault model. Specifically, the maximum earthquake of the synthetic catalog in the AMF corresponds to a complex co-rupture transferred to the LTF (Fig. 3a). Earthquake simulation based on our fault model shows that large ruptures nucleated in the AMF most often tend to propagate along the southern sections and then cease and re-nucleate in parallel segments located at a ~ 7 km distance, instead of rupturing the entire fault length (Herrero-Barbero et al., 2021b). This would be explained by the lower slip rates estimated in the NE sections of the AMF (Herrero-Barbero et al., 2020), which make it difficult the synchronization of the fault sections at their failure limit; and/or by the proximity and orientation of the sections involved, which favor the stress transfer (Oglesby, 2008).

5.2. Influence of the GMPE

The assignment of an attenuation model is other critical point for ground-motion estimation, since there are notable differences between the GMPE, especially for the near-source PGA values. When examining the PGA under rock conditions (Vs_{30} = 750 m/s) with the CB14 attenuation equation (Fig. 8a,b), we observed that the PGA values according to distance are similar in both GMPE, but there are differences of around 0.25 g in the maximum accelerations reached on the fault dipping planes with respect to the AKK14 estimations (see Fig. 8c,d and bottom right plots of Figs. 5 and 6). The CB14 equation considers a hanging wall term dependent of the fault dip and the closest distance to the top edge of rupture that is not fully represented in the AKK14 model. Therefore, the AMF and the BSF are remarkably dependent on the GMPE selected due to their geometry near the source, as previously suggested Benito et al. (2012) and Gómez-Novell et al. (2020). This may result in an under- or overestimation of the values obtained, depending on the case, with a very significant effect at great magnitudes.

There are other phenomena associated with seismic rupture propagation that are not fully represented by the GMPE. The maximum acceleration reached in the 2011, Mw 5.1 Lorca earthquake was 0.36 g in

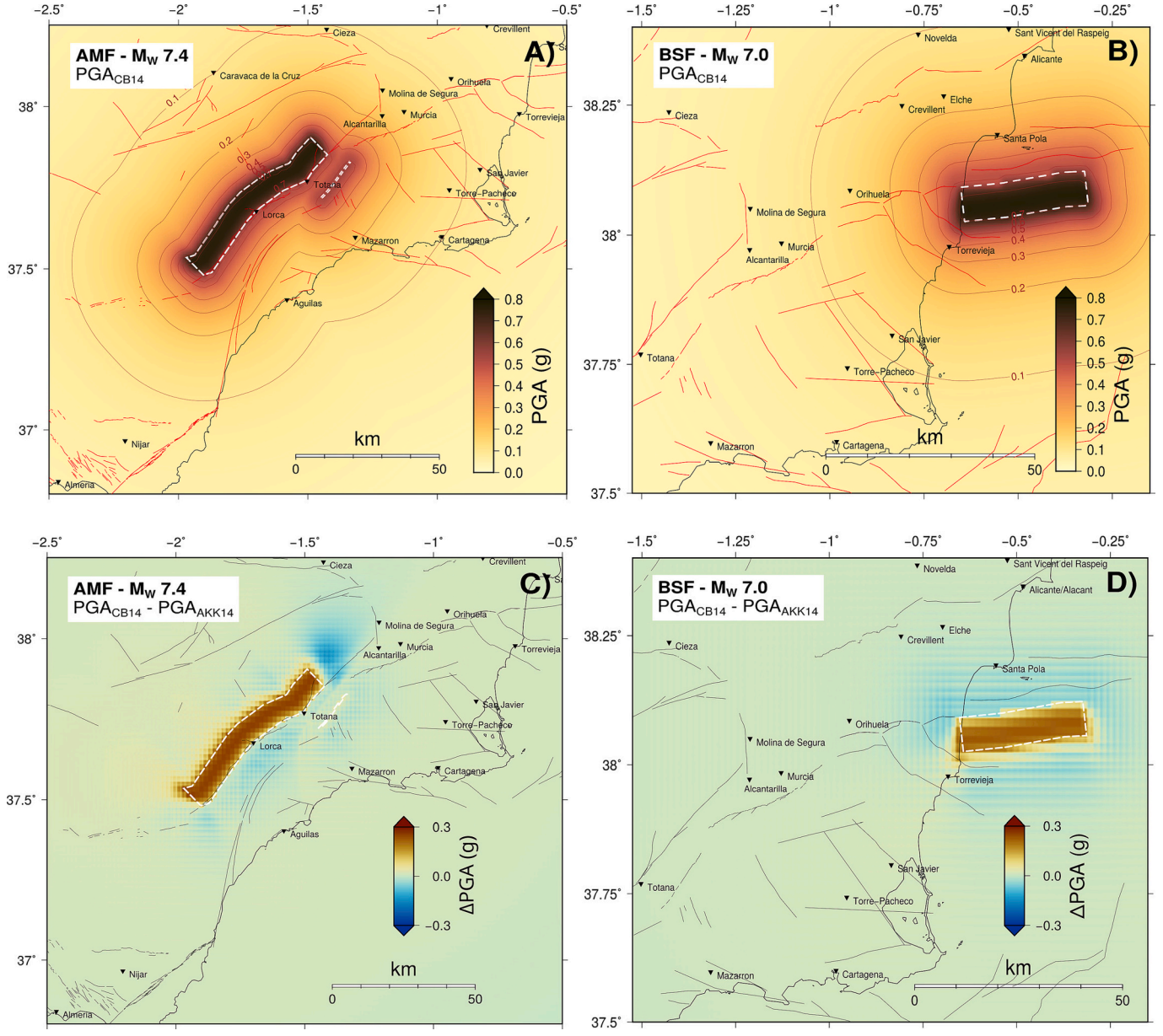

Fig. 8. a) and b) PGA distribution (g) of the estimated maximum events in the Alhama de Murcia (AMF) and Bajo Segura (BSF) faults calculated with the GMPE model of Campbell and Bozorgnia (2014) for a Vs_{30} = 750 m/s. c) and d) the difference ΔPGA with the results under rock conditions calculated with Akkar et al. (2014).

the N—W horizontal component (Cabañas et al., 2014), despite its moderate magnitude, which has been associated to rupture directivity (Gordo-Monsó and Miranda, 2018; López-Comino et al., 2012). Most advanced GMPE do not include a function of rupture directivity effect (Somerville et al., 1997), even though source rupture has a large effect on intensity measures, especially at long-periods (Kuo et al., 2019). Without ignoring a possible underestimation due to the GMPE used, we should also consider that rupture directivity could generate anomalous values in our scenarios, such as those of the 2011 Lorca earthquake.

Simulating the ground motion for complex ruptures is also an issue to take into account when assessing acceleration maps for hazard studies. As we can see in Fig. 5a, although it would not imply an increase in the maximum PGA values reached, complexities would be relevant in the spatial distribution of the PGA and, therefore, in the threat. In this research, we only considered the area dimensions resulting from the representative rupture, since the GMPE only calculates the ground motion from a single magnitude and a rupture area with homogeneous slip. Nevertheless, we observe in the simulations that the displacement on rupture plane is heterogeneous and would be markedly greater in the AMF than in the LTF (Fig. 3a). To overcome this limitation and accurately model ground motion associated with heterogeneous slip along the rupture area, it will be preferable to approach other techniques, such as dynamic models that simulate off-fault deformations and directly predict resulting accelerations (Douilly et al., 2015; Wollherr et al., 2019). In short, it becomes clear that if the modeling of rupture frequencies and areas is sensitive to the geometries and slip rates assigned to faults, so is, logically, the ground-motion simulations in hazard studies.

5.3. Influence of soil amplification in specific populated zones

Among the worst-case estimations of ground motion, we observe that some densely populated areas of the evaluated territory reach maximum peak acceleration values >0.6 g (Fig. 9), either due to the earthquake magnitude, the proximity to the modeled seismic sources, the fault geometry, the concentration of soft soils with high amplification potential, or by the combination of several of these factors. These zones include the Guadalentin corridor, southern Bajo Segura basin along the river bank, and the southeast coast of Alicante province, reaching critical PGA values of between 0.4 and 0.6 g in municipalities with >30 k inhabitants such as Lorca, Murcia (Fig. 5c,d), Orihuela or Torrevieja (Fig. 6c,d).

According to the results obtained in our scenarios, sometimes the combined effect of the proximity to the rupture plane and the soil amplification have a greater impact on the PGA value reached than the earthquake magnitude. Site amplification during an earthquake can be noticeable at large distances even when the calculated PGA on rock is <0.2 g (see e.g. the values in towns such us Mazarron or Elche; Fig. 9); therefore, the threat in certain areas of the territory should not be neglected, even being very far from the source of the maximum earthquake. For example, the worst event in the CAF (M_W 6.9) would generate in the city of Murcia an acceleration of almost 0.6 g (Fig. 6c), similar to that reached in Lorca due to a maximum earthquake M_W 7.4 in the AMF, although the source-to-location distance is smaller (Fig. 5c). In the case of a rupture of the offshore section of the BSF (Fig. 6b), the likely PGA value obtained is notably higher in Orihuela (0.31 ± 0.01 g) than the PGA reached in Elche (0.242 ± 0.004 g), despite the shortest distance of the latter from the epicenter (Fig. 6d). Meanwhile, the maximum acceleration would be reached in the urban area of Torrevieja (0.48 ± 0.06 g), located 8 km from the source and also subject to a moderate local effect. Murcia and Orihuela are predominantly located on highly saturated clay and silt deposits, which we classified as geotechnical soft soil class V and VI (Table 2 and Fig. 4a,b); and Torrevieja is located on thick loamy and sandy soils with high plasticity (class IV-V). These areas located in the Bajo Segura basin (Fig. 4b), where soft soils would tend to favor seismic wave amplification during an earthquake, has also been characterized as highly susceptible to liquefaction (Alfaro et al., 2001; Delgado et al., 2003). These properties would have disastrous consequences in the location of urban infrastructures.

Given the large scale of the study area and the enormously heterogeneous lithology of the Eastern Betics, site-dependent response by the presence of soft soils has been evaluated taking into account the dynamic properties of the materials in the first meters depth. It is not possible to consider, in this case, the anisotropies of the heterogeneous crust, which condition the non-linear response of soils during a large earthquake. It has been shown that non-linear effects, such as an increased damping and a reduced shear wave velocity, can produce strong motion deamplification, specially for PGA values >0.1 g, accompanied by changes in resonance frequencies (Wen et al., 1994). Among the numerical alternatives to be considered in further research, dynamic modeling would allow to reproduce seismic wave propagation and ground accelerations by simulating synthetic seismograms (e.g., Douilly et al., 2015; Wollherr et al., 2019), also considering viscoelastic media and the consequent incorporation of the nonlinear behavior of soils into the simulations (e.g., Bradley, 2019).

We acknowledge that the lack of observed strong motion and near-surface Vs_{30} data to validate the results may lead to the above-mentioned uncertainties of the estimated ground motions. The largest uncertainties will probably derive from the assigning Vs_{30} values from a geothechnical and geology-based proxy (Seyhan et al., 2014). Another proxy to consider to reinforce future Vs_{30} estimations is the topographic slope, as proposed by the recent model by Crespo et al. (2022) for the Iberian Peninsula. Despite the limitations, the characterization of soils carried out in this research makes it possible to delimit some areas of the study region that are susceptible to local effects during a large-magnitude earthquake due to the type of soils, paying special attention to long-distance areas from the source that may experience unexpected amplification. These zones would need a detailed assessment through in-situ characterization of dynamic properties by means of other techniques and local studies. We expect that this evaluation could serve as a guideline of improvement for future strong motion prediction studies in the Eastern Betics.

6. Conclusions

Using physics-based earthquake simulations obtained with the RSQSim quasi-dynamic code (Richards-Dinger and Dieterich, 2012), we explore how large earthquakes would influence the seismic hazard of the northern half of the Eastern Betics (SE Iberia). A detailed long-term catalog of slip events has allowed us to estimate the rupture characteristics associated with the maximum magnitudes of the sources, as well as other severe magnitudes with rare historical precedents. From a deterministic approach and using ground motion equations, we have estimated scenarios of maximum peak accelerations, PGA (g), reached in these synthetic events. Likewise, we consider in our analysis the influence of the soil types and its potential of earthquake-induced motion amplification. For this, we have carried out a detailed geotechnical classification of near-surface geological materials of the Guadalentin and Bajo Segura Quaternary basins, on which densely populated urban areas are located.

The maximum simulated earthquakes obtained from the 100 kyr synthetic catalog for the modeled faults bounding the Guadalentin and Bajo Segura basins are: M_W 7.4 for the Alhama de Murcia Fault (AMF), M_W 6.7 for the Palomares Fault (PF), M_W 6.9 for the Carrascoy Fault (CAF), and M_W 7.1 for the Bajo Segura Fault (BSF). According to the ground motion estimations with Akkar et al. (2014) incorporating our soil amplification factors, the maximum scenario in the AMF (Fig. 5a) would generate the largest extension for PGA > 0.1 g, due to its dipping geometry and a rupture transfer with other near fault of the system. Urban areas located along the Guadalentin valley, such as Lorca, could be subject to site-dependent PGA values close to 0.6 g on the fault trace (Fig. 5c). Similar ground motion values would affect the coastline between the densely populated areas at the SE Alicante province when

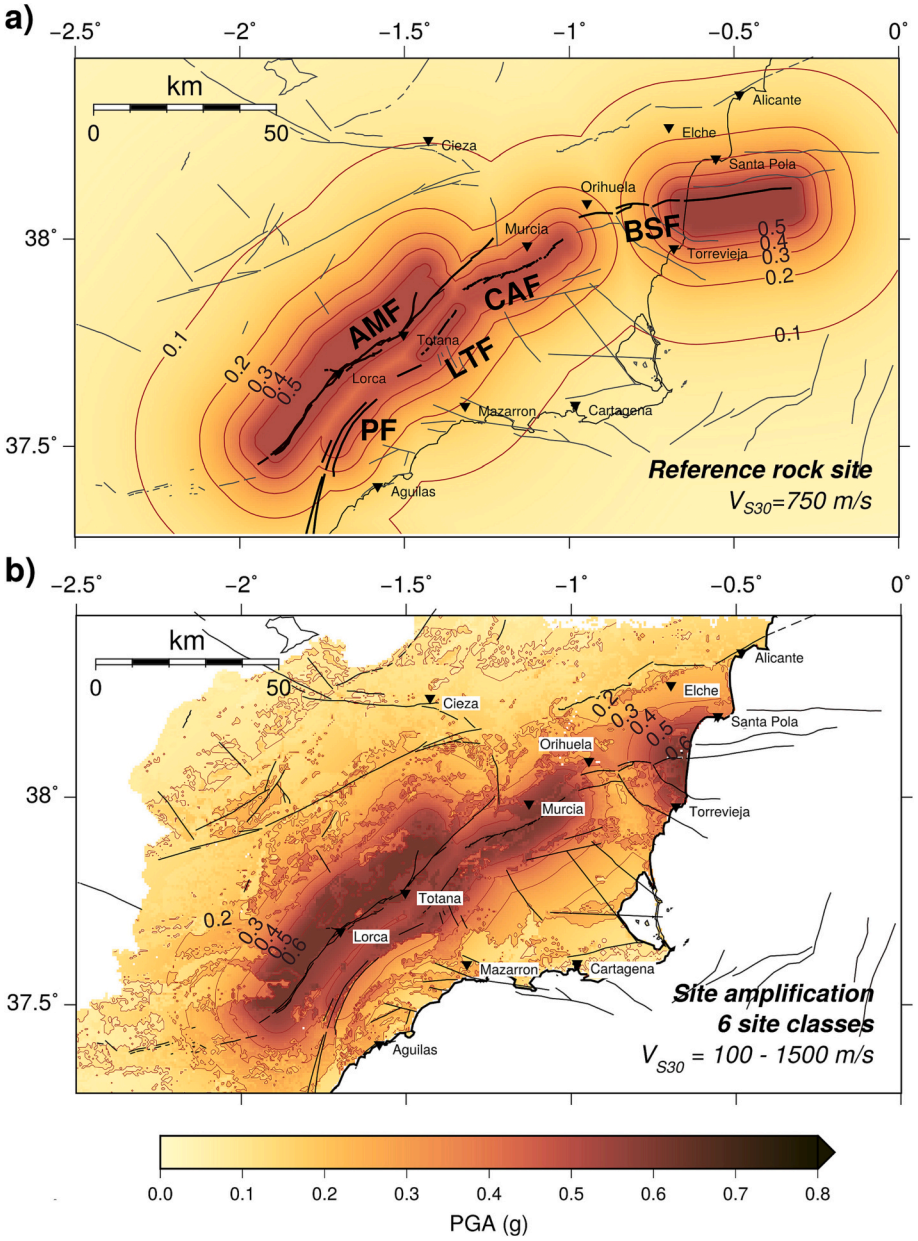

Fig. 9. Maximum PGA scenario (g) resulting from the integration of all estimated worst-case scenarios. We have selected the maximum value of estimated PGA in each pixel of 500 m^2 size. a) Integration of scenarios under rock conditions ($V_S \geq 750$ m/s), without amplification. b) Integration of scenarios involving soil amplification. Labels for the faults names are the same as those in Fig. 1.

evaluating the maximum scenario for the BSF (Fig. 6b,d). However, for smaller magnitudes (M_W 6.2–6.6), the accelerations estimated in the south side of the Bajo Segura Basin already exceed a critical PGA value of 0.5 g (Fig. 7c,d), due to the thick deposits of very soft and saturated clay from the Quaternary alluvial plain, which would probably induce ground-motion amplification. Similar soils are characterized in the northern end of the Guadalentin basin, contributing to a strong site-dependent response in this area where the main city of the region, Murcia, is located. The worst-case scenario for the nearest source, the CAF, estimates a maximum PGA close to 0.6 g on Murcia city (Fig. 6a,c); while the acceleration reached in Murcia for the maximum synthetic earthquake in the AMF would be still significant despite the distance to the hypocenter near Lorca, with a PGA >0.3 g.

Therefore, the combined influence of the earthquake magnitude, fault geometry and the presence of soft soils with high amplification potential could generate, according to our worst-case scenarios, maximum PGA values of ~0.6 g in the city of Murcia and the urban areas located on the Segura river floodplain and the Torrevieja coastline, which are close to important seismogenic faults (Fig. 9). These values could be even greater (>0.7 g) on the fault plane (Fig. 8) if we consider other GMPE that calibrate the influence of fault dip (Campbell and Bozorgnia, 2014), or due to other effects like near-fault rupture directivity that can increase the resulting earthquake-induced ground motion.

Besides the need to overcome the limitations derived from the scarcity of local strong motion records and in-situ Vs_{30} measurements, the estimation of scenarios of large earthquakes, poorly represented in the instrumental and historical catalogs, has great potential for testing the implementation of seismogenic sources in the Probabilistic Seismic Hazard Analysis (PSHA). In addition, the physics-based rupture modeling considers stress interactions between seismic sources in a region. That allows us to address scenarios associated with complex fault

ruptures involving different segments and/or faults, which has implications for the maximum magnitudes and the spatial distribution of seismic hazard.

CRediT authorship contribution statement

Paula Herrero-Barbero: Conceptualization, Data curation, Formal analysis, Investigation, Writing – original draft, Writing – review & editing. **José A. Álvarez-Gómez:** Conceptualization, Funding acquisition, Investigation, Writing – review & editing. **Meaza Tsige:** Conceptualization, Investigation, Writing – review & editing. **José J. Martínez-Díaz:** Conceptualization, Funding acquisition, Investigation, Writing – review & editing.

Declaration of Competing Interest

The authors declare that they have no known competing financial interests or personal relationships that could have appeared to influence the work reported in this paper.

Data availability

Data set with the inputs and results of the simulations is available into a data repository: https://doi.org/10.6084/m9.figshare.12909815 (Herrero-Barbero et al., 2021a). GMT package (Wessel et al., 2013) was used to create some figures.

Acknowledgements

This study was supported by the SHaKER project (PID2021-124155NB-C31) funded by the Ministry of Science and Innovation of Spain. P. Herrero-Barbero thanks the funding support from a Spanish FPU Fellowship. We thank C. Williams, P. Villamor and K. Richards-Dinger for their contribution to physics-based modeling with RSQSim, and J.M. Insua, J. Alonso and J. Mayordomo for their suggestions with the fault data review and the GMPE selection. The authors greatly appreciate the detailed comments and suggestions from the Editor and two anonymous reviewers.

Appendix A. Supplementary data

Supplementary data to this article can be found online at https://doi.org/10.1016/j.enggeo.2023.107364.

References

Aki, K., 1993. Local site effects on weak and strong ground motion. Tectonophysics 218 (1–3), 93–111. https://doi.org/10.1016/0040-1951(93)90262-I.

Akkar, S., Sandıkkaya, M.A., Bommer, J.J., 2014. Empirical ground-motion models for point-and extended-source crustal earthquake scenarios in Europe and the Middle East. Bull. Earthq. Eng. 12 (1), 359–387. https://doi.org/10.1007/s10518-013-9461-4.

Alfaro, P., Delgado, J., Estévez, A., López-Casado, C., 2001. Paleoliquefaction in the Bajo Segura basin (eastern Betic Cordillera). Acta Geol. Hisp. 36 (3), 233–244.

Alfaro, P., Delgado, J., Estévez, A., Soria, J., Yébenes, A., 2002. Onshore and offshore compressional tectonics in the eastern Betic Cordillera (SE Spain). Mar. Geol. 186 (3–4), 337–349. https://doi.org/10.1016/S0025-3227(02)00336-5.

Alfaro, P., Bartolomé, R., Borque, M., Estévez, A., García-Mayordomo, J., García-Tortosa, F., Gil, A., Gràcia, E., Lo Iacono, C., Perea, H., 2012. The Bajo Segura Fault Zone: active blind thrusting in the Eastern Betic Cordillera (SE Spain). J. Iber. Geol. 38 (1), 271–284. https://doi.org/10.5209/rev_JIGE.2012.v38.n1.39217.

Alonso-Henar, J., Benito, B., Staller, A., Álvarez-Gómez, J.A., Martínez-Díaz, J.J., Canora, C., 2018. Large-magnitude crustal seismic sources in El Salvador and deterministic hazard scenarios. Eng. Geol. 243, 70–83. https://doi.org/10.1016/j.enggeo.2018.06.015.

Alonso-Henar, J., Fernández, C., Martínez-Díaz, J. J., 2020. Application of the analytic model of general triclinic transpression with oblique extrusion to an active deformation zone: the Alhama de Murcia Fault (SE Iberian Peninsula). J. Struct. Geol. 130, 103924 https://doi.org/10.1016/j.jsg.2019.103924.

Álvarez-Gómez, J.A., Herrero-Barbero, P., Martínez-Díaz, J.J., 2023. Seismogenic potential and tsunami threat of the strike-slip Carboneras fault in the western Mediterranean from physics-based earthquake simulations. Nat. Hazards Earth Syst. Sci. 23 (6), 2031–2052. https://doi.org/10.5194/nhess-23-2031-2023.

Anbazhagan, P., Abraham, G.S., 2020. Region specific seismic hazard analysis of Krishna Raja Sagara Dam, India. Eng. Geol. 268, 105512.

Anbazhagan, P., Bajaj, K., Moustafa, S.S., Al-Arifi, N.S., 2015. Maximum magnitude estimation considering the regional rupture character. J. Seismol. 19 (3), 695–719.

Aochi, H., Douglas, J., Ulrich, T., 2017. Stress accumulation in the Marmara Sea estimated through ground-motion simulations from dynamic rupture scenarios. J. Geophys. Res. Solid Earth 122 (3), 2219–2235. https://doi.org/10.1002/2016JB013790.

ASCE, 2017. Minimum Design Loads and Associated Criteria for Buildings and Other Structures (7–16) (Standars ASCE/SEI 7–16). American Society of Civil Engineers, Virginia, EE.UU, 690 p.

Benito, B., Capote, R., Murphy, P., Gaspar-Escribano, J.M., Martínez-Díaz, J.J., Tsige, M., Canora, C., 2007. An overview of the damaging and low magnitude Mw 4.8 La Paca earthquake on 29 January 2005: context, seismotectonics, and seismic risk implications for Southeast Spain. Bull. Seismol. Soc. Am. 97 (3), 671–690. https://doi.org/10.1785/0120050150.

Benito, B., Medina, A.R., Escribano, J., Murphy, P., 2012. El terremoto de Lorca (2011) en el contexto de la peligrosidad y el riesgo sísmico en Murcia. Física de la Tierra 24 (2012), 255–287.

Booth-Rea, G., Azañón, J.-M., Azor, A., García-Dueñas, V., 2004. Influence of strike-slip fault segmentation on drainage evolution and topography. A case study: the Palomares Fault Zone (southeastern Betics, Spain). J. Struct. Geol. 26 (9), 1615–1632. https://doi.org/10.1016/j.jsg.2004.01.007.

Borcherdt, R.D., 1994. Estimates of site-dependent response spectra for design (methodology and justification). Earthquake Spectra 10 (4), 617–653. https://doi.org/10.1193/1.1585791.

Borcherdt, R.D., Glassmoyer, G., 1992. On the characteristics of local geology and their influence on ground motions generated by the Loma Prieta earthquake in the San Francisco Bay region, California. Bull. Seismol. Soc. Am. 82 (2), 603–641. https://doi.org/10.1785/BSSA0820020603.

Bousquet, J., 1979. Quaternary strike-slip faults in southeastern Spain. Tectonophysics 52 (1–4), 277–286. https://doi.org/10.1016/0040-1951(79)90232-4.

Bradley, B.A., 2019. On-going challenges in physics-based ground motion prediction and insights from the 2010–2011 Canterbury and 2016 Kaikoura, New Zealand earthquakes. Soil Dyn. Earthq. Eng. 124, 354–364. https://doi.org/10.1016/j.soildyn.2018.04.042.

BSSC, 2015. NEHRP Recommended Provisions for Seismic Regulations for New Buildings and Other Structures (FEMA P-1050-1). Building Seismic Safety Council, Washington, 515 p.

BSSC, 2020. NEHRP Recommended Provisions for Seismic Regulations for New Buildings and Other Structures (FEMA P-2082-1). Building Seismic Safety Council, Washington, 555 p.

Cabañas, L., Alcalde, J.M., Carreño, E., Bravo, J.B., 2014. Characteristics of observed strong motion accelerograms from the 2011 Lorca (Spain) earthquake. Bull. Earthq. Eng. 12 (5), 1909–1932. https://doi.org/10.1007/s10518-013-9501-0.

Campbell, K.W., Bozorgnia, Y., 2014. NGA-West2 ground motion model for the average horizontal components of PGA, PGV, and 5% damped linear acceleration response spectra. Earthquake Spectra 30 (3), 1087–1115. https://doi.org/10.1193/062913EQS175M.

Chen, G., Magistrale, H., Rong, Y., Cheng, J., Ahmet Binselam, S., Xu, X., 2021. Seismic Site Condition of mainland China from Geology. Seismol. Soc. Am. 92 (2A), 998–1010. https://doi.org/10.1785/0220180370.

Console, R., Carluccio, R., Papadimitriou, E., Karakostas, V., 2015. Synthetic earthquake catalogs simulating seismic activity in the Corinth Gulf, Greece, fault system: Corinth earthquakes simulations. J. Geophys. Res. Solid Earth 120 (1), 326–343. https://doi.org/10.1002/2014JB011765.

Cornell, C.A., 1968. Engineering seismic risk analysis. Bull. Seismol. Soc. Am. 58 (5), 1583–1606. https://doi.org/10.1785/BSSA0580051583.

Crespo, M.J., Benjumea, B., Moratalla, J.M., Lacoma, L., Macau, A., González, Á., Stafford, P.J., 2022. A proxy-based model for estimating VS30 in the Iberian Peninsula. Soil Dyn. Earthq. Eng. 155, 107165.

Cruz-Atienza, V., Tago, J., Sanabria-Gómez, J., Chaljub, E., Etienne, V., Virieux, J., Quintanar, L., 2016. Long duration of ground motion in the paradigmatic valley of Mexico. Sci. Rep. 6 (1), 1–9. https://doi.org/10.1038/srep38807.

De Larouzière, F., Bolze, J., Bordet, P., Hernandez, J., Montenat, C., d'Estevou, P.O., 1988. The Betic segment of the lithospheric Trans-Alboran shear zone during the Late Miocene. Tectonophysics 152 (1–2), 41–52. https://doi.org/10.1016/0040-1951(88)90028-5.

Delgado, J., 1997. Zonificación sísmica de la Vega Baja del Río Segura: Análisis de la respuesta del suelo. Doctoral dissertation,. Universidad de Alicante.

Delgado, J., Alfaro, P., Andreu, J., Cuenca, A., Doménech, C., Estévez, A., Yébenes, A., 2003. Engineering-geological model of the Segura River flood plain (SE Spain): a case study for engineering planning. Eng. Geol. 68 (3–4), 171–187. https://doi.org/10.1016/S0013-7952(02)00226-0.

Dieterich, J.H., 1978. Time-dependent friction and the mechanics of stick-slip. In: Rock Friction and Earthquake Prediction. Springer, pp. 790–806.

Dieterich, J.H., 1979. Modeling of rock friction: 1. Experimental results and constitutive equations. J. Geophys. Res. Solid Earth 84 (B5), 2161–2168.

Dieterich, J.H., Richards-Dinger, K.B., 2010. Earthquake recurrence in simulated fault systems. Pure Appl. Geophys. 8 (167), 1087–1104. https://doi.org/10.1007/s00024-010-0094-0.

Dikmen, Ü., 2009. Statistical correlations of shear wave velocity and penetration resistance for soils. J. Geophys. Eng. 6 (1), 61–72.

Dobry, R., Borcherdt, R., Crouse, C., Idriss, I., Joyner, W., Martin, G.R., Seed, R., 2000. New site coefficients and site classification system used in recent building seismic code provisions. Earthquake Spectra 16 (1), 41–67. https://doi.org/10.1193/1.1586082.

Douilly, R., Aochi, H., Calais, E., Freed, A., 2015. Three-dimensional dynamic rupture simulations across interacting faults: the Mw 7.0, 2010, Haiti earthquake. J. Geophys. Res. Solid Earth 120 (2), 1108–1128. https://doi.org/10.1002/2014JB011595.

Fernandes, R., Miranda, J., Meijninger, B., Bos, M., Noomen, R., Bastos, L., Riva, R., 2007. Surface velocity field of the Ibero-Maghrebian segment of the Eurasia-Nubia plate boundary. Geophys. J. Int. 169 (1), 315–324. https://doi.org/10.1111/j.1365-246X.2006.03252.x.

Ferraro, A., Grasso, S., Maugeri, M., Totani, F., 2016. Seismic response analysis in the southern part of the historic Centre of the City of L'Aquila (Italy). Soil Dyn. Earthq. Eng. 88, 256–264. https://doi.org/10.1016/j.soildyn.2016.06.009.

Ferrater, M., Ortuño, M., Masana, E., Martínez-Díaz, J., Pallàs, R., Perea, H., Rockwell, T., 2017. Lateral slip rate of Alhama de Murcia fault (SE Iberian Peninsula) based on a morphotectonic analysis: comparison with paleoseismological data. Quat. Int. 451, 87–100. https://doi.org/10.1016/j.quaint.2017.02.018.

Field, E., Jordan, T., Cornell, C., 2003. OpenSHA: a developing community-modeling environment for seismic hazard analysis. Seismol. Res. Lett. 74 (4), 406–419. https://doi.org/10.1785/gssrl.74.4.406.

Franke, K.W., Candia, G., Mayoral, J.M., Wood, C.M., Montgomery, J., Hutchinson, T., Morales-Velez, A.C., 2019. Observed building damage patterns and foundation performance in Mexico City following the 2017 M7.1 Puebla-Mexico City earthquake. Soil Dyn. Earthq. Eng. 125, 105708 https://doi.org/10.1016/j.soildyn.2019.105708.

García-Fernández, M., Jiménez, M., 2012. Site characterization in the Vega Baja, SE Spain, using ambient-noise H/V analysis. Bull. Earthq. Eng. 10 (4), 1163–1191. https://doi.org/10.1007/s10518-012-9351-1.

García-Mayordomo, J., 2005. Caracterización y Análisis de la Peligrosidad Sísmica en el Sureste de España. Doctoral dissertation.. Universidad Complutense de Madrid.

Gómez-Novell, O., García-Mayordomo, J., Ortuño, M., Masana, E., Chartier, T., 2020. Fault system-based probabilistic seismic hazard assessment of a moderate seismicity region: the Eastern Betics Shear Zone (SE Spain). Front. Earth Sci. 8, 579398 https://doi.org/10.3389/feart.2020.579398.

Gómez-Novell, O., Ortuño, M., García-Mayordomo, J., Insua-Arévalo, J.M., Rockwell, T. K., Baize, S., Masana, E., 2022. Improved geological slip rate estimations in the complex Alhama de Murcia Fault zone (SE Iberia) and its implications for fault behavior. Tectonics 41 e2022TC007465.

Gordo-Monsó, C., Miranda, E., 2018. Significance of directivity effects during the 2011 Lorca earthquake in Spain. Bull. Earthq. Eng. 16 (7), 2711–2728. https://doi.org/10.1007/s10518-017-0301-9.

Herrero-Barbero, P., Álvarez-Gómez, J.A., Martínez-Díaz, J.J., Klimowitz, J., 2020. Neogene basin inversion and recent slip rate distribution of the northern termination of the Alhama de Murcia Fault (Eastern Betic Shear Zone, SE Spain). Tectonics 39. https://doi.org/10.1029/2019TC005750 e2019TC005750.

Herrero-Barbero, P., Álvarez-Gómez, J., Williams, C., Villamor, P., Insua-Arévalo, J., Alonso-Henar, J., Martínez-Díaz, J., 2021a. DATASET - Physics-based earthquake simulations in slow-moving faults: a case study from the Eastern Betic Shear Zone (SE Spain). In: Figshare Data Repository. https://doi.org/10.6084/m9.figshare.12909815.

Herrero-Barbero, P., Álvarez-Gómez, J., Williams, C., Villamor, P., Insua-Arévalo, J., Alonso-Henar, J., Martínez-Dıaz, J., 2021b. Physics-based earthquake simulations in slow-moving faults: a case study from the Eastern Betic Shear Zone (SE Iberian Peninsula). J. Geophys. Res. Solid Earth 126 (5). https://doi.org/10.1029/2020JB021133 e2020JB021133.

IGME, 1973. Mapa Geotécnico General a escala 1:200.000. Mapa de interpretación geotécnica. In: Hoja 72 (7-9) - Elche. Instituto Geológico y Minero de España (IGME).

IGME, 1977. Mapa Geotécnico General a escala 1:200.000. Mapa de interpretación geotécnica. In: Hoja 70 (7-10) - Murcia. Instituto Geológico y Minero de España (IGME).

IGME, 1984. Mapa Geotécnico y de Riesgos Geológicos de la ciudad de Murcia. In: Mapa Geotécnico y de Riesgos Geológicos 25k y 5k. Instituto Geológico y Minero de España (IGME).

IGME, 2000. Estudio de los recursos subterraneos de agua salobre en la zona sur de la provincia de Alicante. Instituto Geológico y Minero de España IGME, 437.

IGN-UPM, 2013. Actualización de mapas de peligrosidad sísmica de España 2012. Centro Nacional de Información Geográfica, 267.

Imai, T., 1977. P-and S-wave velocities of the ground in Japan. Proc. IX Int. Conf. Soil Mech. Found. Eng. 2, 127–132.

Insua-Arévalo, J.M., García-Mayordomo, J., Salazar, A., Rodríguez-Escudero, E., Martín-Banda, R., Álvarez-Gómez, J.A., Martínez-Díaz, J.J., 2015. Paleoseismological evidence of Holocene activity of the Los Tollos Fault (Murcia, SE Spain): a lately formed Quaternary tectonic feature of the Eastern Betic Shear Zone. J. Iber. Geol. 41 (3), 333–350.

Joyner, W.B., Boore, D.M., 1981. Peak horizontal acceleration and velocity from strong-motion records including records from the 1979 Imperial Valley, California, earthquake. Bull. Seismol. Soc. Am. 71 (6), 2011–2038.

Kijko, A., Graham, G., 1998. Parametric-historic procedure for probabilistic seismic hazard analysis part I: estimation of maximum regional magnitude mmax. Pure Appl. Geophys. 152 (3), 413–442.

Koulali, A., Ouazar, D., Tahayt, A., King, R., Vernant, P., Reilinger, R., Amraoui, N., 2011. New GPS constraints on active deformation along the Africa–Iberia plate boundary. Earth Planet. Sci. Lett. 308 (1–2), 211–217. https://doi.org/10.1016/j.epsl.2011.05.048.

Kuo, C.H., Huang, J.Y., Lin, C.M., Hsu, T.Y., Chao, S.H., Wen, K.L., 2019. Strong ground motion and pulse-like velocity observations in the near-fault region of the 2018 Mw 6.4 Hualien, Taiwan earthquake. Seismol. Res. Lett. 90 (1), 40–50.

Leonard, M., 2010. Earthquake fault scaling: self-consistent relating of rupture length, width, average displacement, and moment release. Bull. Seismol. Soc. Am. 100 (5A), 1971–1988. https://doi.org/10.1785/0120090189.

López-Comino, J.A., Mancilla, F. d L., Morales, J., Stich, D., 2012. Rupture directivity of the 2011, Mw 5.2 Lorca earthquake (Spain). Geophys. Res. Lett. 39, 3. https://doi.org/10.1029/2011GL050498.

Magrin, A., Peresan, A., Kronrod, T., Vaccari, F., Panza, G.F., 2017. Neo-deterministic seismic hazard assessment and earthquake occurrence rate. Eng. Geol. 229, 95–109.

Martín-Banda, R., García-Mayordomo, J., Insua-Arévalo, J.M., Salazar, Á.E., Rodríguez-Escudero, E., Álvarez-Gómez, J.A., Herrero, M.J., 2016. New insights on the seismogenic potential of the Eastern Betic Shear Zone (SE Iberia): Quaternary activity and paleoseismicity of the SW segment of the Carrascoy Fault Zone. Tectonics 35 (1), 55–75. https://doi.org/10.1002/2015TC003997.

Martín-Banda, R., Insua-Arévalo, J.M., García-Mayordomo, J., 2021. Slip rate variation during the last~ 210 ka on a slow fault in a transpressive regime: the Carrascoy Fault (Eastern Betic Shear Zone, SE Spain). Front. Earth Sci. 8, 599608 https://doi.org/10.3389/feart.2020.599608.

Martínez-Díaz, J.J., Masana, E., Hernández-Enrile, J.L., Santanach, P., 2001. Evidence for coseismic events of recurrent prehistoric deformation along the Alhama de Murcia fault, southeastern Spain. Acta Geol. Hisp. 315–327.

Martínez-Díaz, J.J., Rodríguez-Pascual, M.Á., Perez López, R., García Mayordomo, J., Giner Robles, J.L., Martín-González, F., Insua Arévalo, M., 2011. Informe geológico preliminar del terremoto de Lorca del 11 de mayo de 2011, 5.1 Mw. Instituto Geológico y Minero de España (IGME-CSIC).

Martínez-Díaz, J.J., Bejar-Pizarro, M., Álvarez-Gómez, J.A., de Lis Mancilla, F., Stich, D., Herrera, G., Morales, J., 2012a. Tectonic and seismic implications of an intersegment rupture: the damaging May 11th 2011 Mw 5.2 Lorca, Spain, earthquake. Tectonophysics 546, 28–37. https://doi.org/10.1016/j.tecto.2012.04.010.

Martínez-Díaz, J.J., Masana, E., Ortuño, M., 2012b. Active tectonics of the Alhama de Murcia fault, Betic Cordillera, Spain. J. Iber. Geol. 38 (1), 253–270. https://doi.org/10.5209/rev_JIGE.2012.v38.n1.39218.

Martínez-Díaz, J.J., Alonso-Henar, J., Insua-Arévalo, J.M., Canora, C., García-Mayordomo, J., Rodríguez-Escudero, E., Masana, E., 2018. Geological evidences of surface rupture related to a seventeenth century destructive earthquake in Betic Cordillera (SE Spain): constraining the seismic hazard of the Alhama de Murcia fault. J. Iber. Geol. 45 (1), 73–86. https://doi.org/10.1007/s41513-018-0082-2.

Martínez-Solares, J., Mezcua, J., 2002. Catálogo sísmico de la Península Ibérica (880 aC-1900). In: Instituto Geográfico Nacional–Monografía, p. 444 (18).

Masana, E., Martínez-Díaz, J.J., Hernández-Enrile, J., Santanach, P., 2004. The Alhama de Murcia fault (SE Spain), a seismogenic fault in a diffuse plate boundary: Seismotectonic implications for the Ibero-Magrebian region. Journal of Geophysical Research: Solid. Earth 109 (B1). https://doi.org/10.1029/2002JB002359.

Meijninger, B., Vissers, R., 2006. Miocene extensional basin development in the Betic Cordillera, SE Spain revealed through analysis of the Alhama de Murcia and Crevillente Faults. Basin Res. 18 (4), 547–571. https://doi.org/10.1111/j.1365-2117.2006.00308.x.

Milner, K.R., Shaw, B.E., Field, E.H., 2022. Enumerating plausible multifault ruptures in complex fault systems with physical constraints. Bull. Seismol. Soc. Am. 112 (4), 1806–1824.

Montenat, C., 1973. Les formations neogènes et quaternaires du levant espagnol: Provinces d'Alicante et de Murcia (Doctoral dissertation, Centre d'Orsay: Université de Paris Sud).

Montenat, C., d'Estevou, P.O., 1999. The diversity of late Neogene sedimentary basins generated by wrench faulting in the eastern Betic Cordillera, SE Spain. J. Pet. Geol. 22 (1), 61–80. https://doi.org/10.1111/j.1747-5457.1999.tb00459.x.

Moreno, X., Masana, E., Pallàs, R., Gràcia, E., Rodés, Á., Bordonau, J., 2015. Quaternary tectonic activity of the Carboneras Fault in the La Serrata range (SE Iberia): Geomorphological and chronological constraints. Tectonophysics 663, 78–94. https://doi.org/10.1016/j.tecto.2015.08.016.

Niemeijer, A.R., Vissers, R.L., 2014. Earthquake rupture propagation inferred from the spatial distribution of fault rock frictional properties. Earth Planet. Sci. Lett. 396, 154–164. https://doi.org/10.1016/j.epsl.2014.04.010.

Nocquet, J.-M., 2012. Present-day kinematics of the Mediterranean: A comprehensive overview of GPS results. Tectonophysics 579, 220–242. https://doi.org/10.1016/j.tecto.2012.03.037.

Oglesby, D., 2008. Rupture termination and jump on parallel offset faults. Bull. Seismol. Soc. Am. 98 (1), 440–447. https://doi.org/10.1785/0120070163.

Okada, Y., 1992. Internal deformation due to shear and tensile faults in a half-space. Bull. Seismol. Soc. Am. 82 (2), 1018–1040.

Ortuño, M., Masana, E., García-Meléndez, E., Martínez-Díaz, J., Štěpančíková, P., Cunha, P.P., Murray, A.S., 2012. An exceptionally long paleoseismic record of a slow-moving fault: the Alhama de Murcia fault (Eastern Betic shear zone, Spain). GSA Bull. 124 (9–10), 1474–1494. https://doi.org/10.1130/B30558.1.

Perea, H., Gràcia, E., Alfaro, P., Bartolomé, R., Lo Iacono, C., Moreno, X., Team, E.S., 2012. Quaternary active tectonic structures in the offshore Bajo Segura basin (SE Iberian Peninsula–Mediterranean Sea). Nat. Hazards Earth Syst. Sci. 12 (10), 3151–3168. https://doi.org/10.5194/nhess-12-3151-2012.

Pérez-Santisteban, I., Martín, A.M., Carbó, A., Ruiz-Fonticiella, J.M., 2016, September. Empirical correlation of shear wave velocity (vs) with spt of soils in Madrid. In: Near Surface Geoscience 2016-22nd European Meeting of Environmental and Engineering Geophysics. European Association of Geoscientists & Engineers (Vol. 2016, No. 1, pp. cp-495).

Ramírez-Gaytan, A., Estrella, H.F., Preciado, A., Bandy, W.L., Lazcano, S., Nolasco, L.A., Korn, M., 2020. Subsoil classification and geotechnical zonation for Guadalajara City, México: Vs30, soil fundamental periods, 3D structure and profiles. Near Surface Geophys. 18 (2), 175–188. https://doi.org/10.1002/nsg.12085.

Richards-Dinger, K., Dieterich, J.H., 2012. RSQSim Earthquake Simulator. Seismol. Res. Lett. 83 (6), 983–990. https://doi.org/10.1785/0220120105.

Rivas-Medina, A., Benito, B., Gaspar-Escribano, J.M., 2018. Approach for combining fault and area sources in seismic hazard assessment: application in South-Eastern Spain. Nat. Hazards Earth Syst. Sci. 18 (11), 2809–2823. https://doi.org/10.5194/nhess-18-2809-2018.

Robinson, R., Benites, R., 1995. Synthetic seismicity models of multiple interacting faults. J. Geophys. Res. Solid Earth 100 (B9), 18229–18238. https://doi.org/10.1029/95JB01569.

Robinson, R., Van Dissen, R., Litchfield, N., 2011. Using synthetic seismicity to evaluate seismic hazard in the Wellington region, New Zealand: synthetic seismicity to evaluate seismic hazard. Geophys. J. Int. 187 (1), 510–528. https://doi.org/10.1111/j.1365-246X.2011.05161.x.

Rodríguez-Escudero, E., 2017. Implicaciones de la Estructura Interna de una Zona de Falla Activa en la Génesis de Terremotos (Doctoral dissertation, Universidad Autónoma de Madrid).

Rosa-Cintas, S., Galiana-Merino, J., Molina-Palacios, S., Rosa-Herranz, J., García-Fernández, M., Jiménez, M., 2011. Soil characterization in urban areas of the Bajo Segura Basin (Southeast Spain) using H/V, F–K and ESAC methods. J. Appl. Geophys. 75 (3), 543–557. https://doi.org/10.1016/j.jappgeo.2011.07.019.

Ruina, A., 1983. Slip instability and state variable friction laws. J. Geophys. Res. Solid Earth 88 (B12), 10359–10370. https://doi.org/10.1029/JB088iB12p10359.

Rundle, J.B., 1988. A physical model for earthquakes: 2. Application to southern California. J. Geophys. Res. Solid Earth 93 (B6), 6255–6274. https://doi.org/10.1029/JB093iB06p06255.

Sanz de Galdeano, C., 1990. Geologic evolution of the Betic Cordilleras in the Western Mediterranean, Miocene to the present. Tectonophysics 172 (1–2), 107–119. https://doi.org/10.1016/0040-1951(90)90062-D.

Seed, H., Ugas, C., Lysmer, J., 1976. Site-dependent spectra for earthquake-resistant design. Bull. Seismol. Soc. Am. 66 (1), 221–243. https://doi.org/10.1785/BSSA0660010221.

Semblat, J.F., Kham, M., Parara, E., Bard, P.-Y., Pitilakis, K., Makra, K., Raptakis, D., 2005. Seismic wave amplification: Basin geometry vs soil layering. Soil Dyn. Earthq. Eng. 25 (7–10), 529–538. https://doi.org/10.1016/j.soildyn.2004.11.003.

Seyhan, E., Stewart, J.P., Ancheta, T.D., Darragh, R.B., Graves, R.W., 2014. NGA-West2 site database. Earthquake spectra 30 (3), 1007–1024.

Shaw, B.E., 2019. Beyond backslip: improvement of earthquake simulators from new hybrid loading conditions beyond backslip: improvement of earthquake simulators from new hybrid loading conditions. Bull. Seismol. Soc. Am. 109 (6), 2159–2167.

Shaw, B.E., Milner, K.R., Field, E.H., Richards-Dinger, K., Gilchrist, J.J., Dieterich, J.H., Jordan, T.H., 2018. A physics-based earthquake simulator replicates seismic hazard statistics across California. Sci. Adv. 4 (8), eaau0688. https://doi.org/10.1126/sciadv.aau0688.

Shaw, B.E., Fry, B., Nicol, A., Howell, A., Gerstenberger, M., 2022. An earthquake simulator for New Zealand. Bull. Seismol. Soc. Am. 112 (2), 763–778. https://doi.org/10.1785/0120210087.

Somerville, P.G., Smith, N.F., Graves, R.W., Abrahamson, N.A., 1997. Modification of empirical strong ground motion attenuation relations to include the amplitude and duration effects of rupture directivity. Seismol. Res. Lett. 68 (1), 199–222.

Stewart, J.P., Seyhan, E., 2013. Semi-Empirical Nonlinear Site Amplification and its Application in NEHRP Site Factors, PEER Report 2013-13. Pacific Earthquake Engineering Research Center, University of California, Berkeley, CA. https://peer.berkeley.edu/sites/default/files/webpeer-2013-13jonathan_p._stewart_and_emel_seyhan.pdf.

Street, R., Woolery, E., Wang, Z., Harik, I., 1997. Soil classifications for estimating site-dependent response spectra and seismic coefficients for building code provisions in western Kentucky. Eng. Geol. 46 (3–4), 331–347. https://doi.org/10.1016/S0013-7952(97)00010-0.

Tomás-Jover, R., 2009. Estudio de la subsidencia de la ciudad de Murcia mediante interferometrıa sar diferencial avanzada (Tesis doctoral, Universitat d'Alacant-Universidad de Alicante).

Tsiambaos, G., Sabatakakis, N., 2011. Empirical estimation of shear wave velocity from in situ tests on soil formations in Greece. Bull. Eng. Geol. Environ. 70 (2), 291–297.

Tsige, M., García Flórez, I., 2006. Propuesta de clasificación geotécnica del "Efecto Sitio"(Amplificación Sísmica) de las formaciones geológicas de la Región de Murcia. Geogaceta 40, 39–42.

Valentini, A., Visini, F., Pace, B., 2017. Integrating faults and past earthquakes into a probabilistic seismic hazard model for peninsular Italy. Nat. Hazards Earth Syst. Sci. 17 (11) https://doi.org/10.5194/nhess-17-2017-2017.

Wang, S., Hao, H., 2002. Effects of random variations of soil properties on site amplification of seismic ground motions. Soil Dyn. Earthq. Eng. 22 (7), 551–564. https://doi.org/10.1016/S0267-7261(02)00038-6.

Wells, D.L., Coppersmith, K., 1994. New empirical relationships among magnitude, rupture length, rupture width, rupture area, and surface displacement. Bull. Seismol. Soc. Am. 84 (4), 974–1002. https://doi.org/10.1785/BSSA0840040974.

Wen, K.-L., Beresnev, I.A., Yeh, Y.T., 1994. Nonlinear soil amplification inferred from downhole strong seismic motion data. Geophys. Res. Lett. 21 (24), 2625–2628. https://doi.org/10.1029/94GL02407.

Wessel, P., Smith, W.H., Scharroo, R., Luis, J., Wobbe, F., 2013. Generic mapping tools: improved version released. EOS Trans. Am. Geophys. Union 94 (45), 409–410. https://doi.org/10.1002/2013EO450001.

Wollherr, S., Gabriel, A.-A., Mai, P.M., 2019. Landers 1992 "reloaded": Integrative dynamic earthquake rupture modeling. J. Geophys. Res. Solid Earth 124 (7), 6666–6702. https://doi.org/10.1029/2018JB016355.

Worden, C.B., Gerstenberger, M.C., Rhoades, D.A., Wald, D.J., 2012. Probabilistic relationships between ground-motion parameters and modified Mercalli intensity in California. Bull. Seismol. Soc. Am. 102 (1), 204–221.